

# JET PROPAGATIONS, BREAKOUTS, AND PHOTOSPHERIC EMISSIONS IN COLLAPSING MASSIVE PROGENITORS OF LONG-DURATION GAMMA-RAY BURSTS

HIROKI NAGAKURA<sup>1</sup>, HIROTAKA ITO<sup>2</sup>, KENTA KIUCHI<sup>3</sup>, AND SHOICHI YAMADA<sup>1,4</sup>

<sup>1</sup> Department of Science and Engineering, Waseda University, 3-4-1 Okubo, Shinjuku, Tokyo 169-8555, Japan; [hiroki@heap.phys.waseda.ac.jp](mailto:hiroki@heap.phys.waseda.ac.jp)

<sup>2</sup> Department of Aerospace Engineering, Tohoku University, 6-6-01 Aramaki-Aza-Aoba, Aoba-ku, Sendai 980-8579, Japan

<sup>3</sup> Yukawa Institute for Theoretical Physics, Kyoto University, Kyoto 606-8502, Japan

<sup>4</sup> Advanced Research Institute for Science and Engineering, Waseda University, 3-4-1 Okubo, Shinjuku, Tokyo 169-8555, Japan

Received 2011 January 14; accepted 2011 February 16; published 2011 March 25

## ABSTRACT

We investigate the following by two-dimensional axisymmetric relativistic hydrodynamical simulations: (1) jet propagations through an envelope of a rapidly rotating and collapsing massive star, which is supposed to be a progenitor of long-duration gamma-ray bursts (GRBs); (2) breakouts and subsequent expansions into stellar winds; and (3) the accompanying photospheric emissions. We find that if the envelope rotates uniformly almost at the mass shedding limit, its outer part eventually stops contracting when the centrifugal force becomes large enough. Then another shock wave is formed, propagates outward, and breaks out of the envelope into the stellar wind. Whether the jet or the centrifugal bounce-induced shock breaks out earlier depends on the timing of jet injection. If the shock breakout occurs earlier, owing to a later injection, the jet propagation and subsequent photospheric emissions are affected substantially. We pay particular attention to observational consequences of the difference in the timing of jet injection. We calculate optical depths to find the location of photospheres, extracting densities, and temperatures at appropriate retarded times from the hydrodynamical data. We show that the luminosity and observed temperature of the photospheric emissions are both much lower than those reported in previous studies. Although luminosities are still high enough for GRBs, the observed temperatures are lower than the energy at the spectral peak expected by the Yonetoku relation. This may imply that energy exchanges between photons and matter are terminated deeper inside or that some non-thermal processes are operating to boost photon energies.

*Key words:* black hole physics – hydrodynamics – radiation mechanisms: general – supernovae: general

*Online-only material:* color figures

## 1. INTRODUCTION

There is mounting observational evidence that links gamma-ray bursts (GRBs) to the death of massive stars (Woosley & Bloom 2006), and it is widely believed that GRBs are associated with the formation of a black hole or a magnetar via the collapse of rapidly rotating massive stars (Woosley 1993; Paczynski 1998; MacFadyen & Woosley 1999). Although we do not know exactly how a large amount of energy is generated, the most promising scenario is that a relativistic jet is launched from the central engine by neutrino annihilation or magnetohydrodynamical processes, propagates through a progenitor star and stellar wind (MacFadyen & Woosley 1999), and then dissipates its kinetic energy by shocks or relativistic turbulences (Piran 2004; Pe’er 2008; Lazzati et al. 2009; Lazar et al. 2009; Kumar & Narayan 2009), producing the prompt emissions of GRBs or X-ray flashes.

A large number of numerical works have been devoted so far to the understanding of relativistic jet propagations in the stellar envelope (Aloy et al. 2000; Zhang et al. 2003, 2004; Mizuta et al. 2006; Mizuta & Aloy 2009; Morsony et al. 2007; Tominaga et al. 2007; Lazzati et al. 2009; Mizuta et al. 2010b). These simulations have demonstrated that the jet is confined by the pressure of a hot cocoon as it penetrates through the stellar envelope. The Kelvin–Helmholtz instability, which occurs between the cocoon and the jet, produces rich internal structures (Lazzati & Begelman 2005; Morsony et al. 2007). More recently, Lazzati et al. (2009) and Mizuta et al. (2010b) computed the jet propagation beyond the stellar surface and observed that these internal structures in the

jet and cocoon leave their traces until later times. They also claimed that the hot jet produces very bright and highly efficient photospheric emissions in the prompt phase of GRBs. These very efficient photospheric emissions may solve the efficiency problem of the prompt emission (Ioka et al. 2007). Interestingly, thermal emissions were indeed recently identified for some long GRBs (Abdo et al. 2009; Ryde et al. 2010; Guiriec et al. 2010). The photospheric emissions from the relativistic jet are hence attracting much attention from the GRB society these days (Pe’er 2008; Toma et al. 2010; Ioka 2010).

It should be noted that the previous numerical studies on the jet propagation ignored the infall of the stellar envelope. According to the collapsar model, on which this paper is based, the gravitational core collapse sets in just like ordinary supernovae when the density reaches  $\rho \sim 10^{9.5} \text{ g cm}^{-3}$  or the temperature exceeds  $T \sim 5 \times 10^9 \text{ K}$  and electron captures or endothermic photodissociations of nuclei reduce pressure (see, e.g., Kotake et al. 2006). A shock wave produced by core bounce stalls in the core and a large amount of matter accretes on a timescale of seconds onto a proto-neutron star at first and into a black hole later. The so-called prompt shock wave either remains stagnated near the black hole or is swallowed into it. The core collapse produces a rarefaction wave at the boundary of the core and envelope, which then propagates outward through the envelope and induces the infall of the envelope when it arrives. Thus, neglecting the envelope motion in studying the jet propagation is justified only when the jet is launched very early on, possibly soon after the black hole is formed (MacFadyen et al. 2001; Zhang et al. 2003), and the infall of

the envelope is not yet substantial. If the jet launch is delayed somehow, on the other hand, the profile of the envelope will be modified and the jet propagation will be affected. The stellar envelope may also eventually cease to infall. In fact, the outer portion of the stellar envelope is likely to have an angular momentum large enough to terminate the infall by centrifugal forces (Woosley & Heger 2006). Indeed, Lindner et al. (2010) observed in their long-term simulations of rotational collapse of massive stars that a shock wave is generated by centrifugal forces and the outer portion of the stellar envelope is eventually expelled. Since we do not know exactly when the jet is launched, it is important to study the influence of envelope dynamics on the jet propagation and subsequent prompt emissions.

Motivated by these facts, we numerically investigate the relativistic jet propagations through a non-stationary envelope, moving either inward or outward, of a rapidly rotating massive star, varying the timing of jet injection. We assume that the prompt shock wave of the core bounce origin has already been swallowed into the black hole and what is supposed to occur in the core after bounce, such as neutrino heating and various hydrodynamical instabilities, does not affect the dynamics of the envelope. We do not specify the mechanism of the jet launch from the central engine, which is under controversy at present, and inject the jet with appropriate properties from the computational inner boundary by hand, following the common practice in this field. Our focus is on the jet propagations in the non-stationary envelope and its influences on the subsequent photospheric emissions. This paper is organized as follows. In Section 2, we describe the models and numerical procedures. We present our main results in Section 3. We conclude the paper with the summary of our findings in Section 4.

## 2. METHODS

As mentioned above, in this paper we compute the jet propagations through the envelope of a rotating massive star into a stellar wind, taking into account the core-collapse-induced motions of the envelope under the assumption that the prompt shock wave is soon sucked into the black hole and various processes in the core such as neutrino heating of accreting matter and hydrodynamical instabilities do not affect the dynamics of the envelope. In order to simulate the infall of the envelope induced by the rarefaction wave that is generated by core collapse, we take rather involved multiple steps. More specifically, we (1) construct massive star envelope models in rotational equilibrium; (2) put quasi-steady winds on top of them; (3) simulate rotational collapse of the envelope, generating a rarefaction wave by artificially reducing the pressure gradient at the inner boundary; (4) compute subsequent jet propagations in the envelope; and (5) calculate photospheric emissions as a postprocess. We employ the so-called HSCF scheme in the first step and perform two-dimensional (2D) relativistic hydrodynamical simulations in the third and fourth steps. In the following, we explain what is done at each step in more detail in order to facilitate the reader's understanding of our results in the next section.

### 2.1. A Massive Star Envelope in Rotational Equilibrium

The first step is a preparation of the initial model for dynamical simulations in the later phases. In this subsection, we construct a 2D axisymmetric model of a rotating massive star envelope in dynamical equilibrium. We employ the method developed by Hachisu (1986) and Kiuchi et al. (2010). It should

be noted here that currently the most elaborate stellar evolution models are still unable to fully implement rotational equilibrium and neglect the non-spherical deformation of rotating stars. In this study, however, the rotational equilibrium is crucial, since the infall of the envelope commences only after the rarefaction wave generated at the boundary of the core and envelope arrives. If the initial model is not in dynamic equilibrium, however, even outer parts of the envelope begin to move immediately after the simulation is started and, more often than not, false shock waves are produced as a consequence.

Our envelope model is constructed so as to mimic the 16TI model by Woosley & Heger (2006), which is currently supposed to be one of the most promising GRB progenitor models. Since the outer envelope of 16TI is almost radiation dominated, we employ a polytropic equation of state (EOS) with the adiabatic index of  $\gamma = 4/3$ . We impose a rigid rotation as an approximation to the outer envelope of 16TI. Figure 1 shows the density profiles on the rotational axis and equator for our model together with the one for 16TI. Also displayed in the figure is the density distribution in the meridian section for our model. Our model agrees fairly well with 16TI except in the innermost portion, where the rotation is not rigid in 16TI. This discrepancy is not very important for the investigation in this study, since that part is sucked into the inner boundary much earlier than the jet injection. Our envelope model has a total mass of  $M \simeq 14 M_\odot$  and a specific angular momentum of  $j_{\text{sp}} \simeq 1.5 \times 10^{19} \text{ cm}^2 \text{ s}^{-1}$  at the stellar surface, which is close to the mass shedding limit. The rotation velocities of our model are slightly lower than those of 16TI in general. The specific angular momentum distribution on the equatorial plane as a function of enclosed mass is shown in Figure 2. Here the enclosed mass is defined as a mass within a certain radius. Also presented in this figure is the specific angular momenta at the innermost stable circular orbit (ISCO) for Schwarzschild black holes as a function of their masses. The two curves intersect with each other at the enclosed mass of  $\sim 8 M_\odot$ . Envelope matter that has a larger enclosed mass than this value cannot fall down to the black hole and is halted somewhere outside the ISCO by centrifugal forces. As a matter of fact, we find a centrifugal bounce and the formation and subsequent propagation of a shock wave (see Section 2.4).

### 2.2. Special Relativistic Hydrodynamic Code

Before proceeding to subsequent steps, we describe the numerical methods employed for the hydrodynamic simulations done in Steps 2–4. We employ a 2D axisymmetric, special relativistic hydrodynamics code. Equatorial symmetry is also assumed in this paper. The basic equations we solve in this study are given as follows in the geometrical units  $G = c = 1$ , where  $G$  and  $c$  are the gravitational constant and speed of light:

$$\partial_t \rho_* + \partial_j (\rho_* v^j) = 0, \quad (1)$$

$$\begin{aligned} \partial_t S_r + \partial_j (r^2 \sin \theta T_r^j) = \\ r^2 \sin \theta \{-T^{00} \psi_{,r} + r T^{\theta\theta} + r \sin^2 \theta T^{\phi\phi}\}, \end{aligned} \quad (2)$$

$$\begin{aligned} \partial_t S_\theta + \partial_j (r^2 \sin \theta T_\theta^j) = \\ r^2 \sin \theta \{-T^{00} \psi_{,\theta} + r^2 \sin \theta \cos \theta T^{\phi\phi}\}, \end{aligned} \quad (3)$$

$$\partial_t S_\phi + \partial_j (r^2 \sin \theta T_\phi^j) = 0, \quad (4)$$

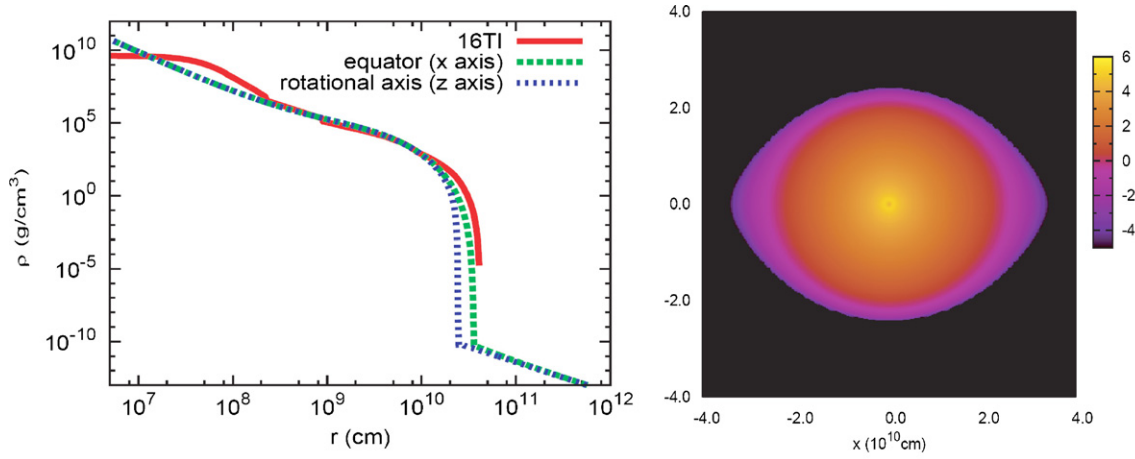


**Figure 1.** Density profiles on the rotational axis (z-axis) and equator (x-axis) for the envelope model in this paper and model 16TI by Woosley & Heger (2006, left panel), and the density contour (log scale) in the meridional section of the same envelope model (right panel).

(A color version of this figure is available in the online journal.)

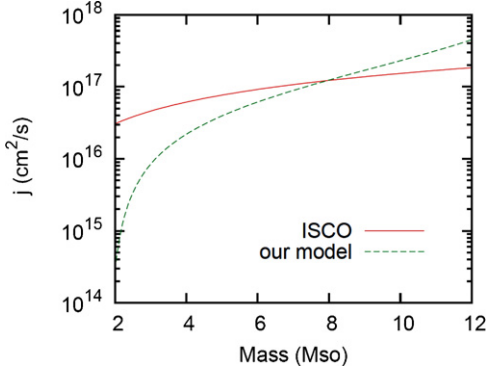


**Figure 2.** Profile of specific angular momentum on the equatorial plane for the envelope model in this paper as a function of included mass (green line). The red line shows the specific angular momenta at the innermost stable circular orbit (ISCO) for Schwarzschild black holes as a function of their masses.

(A color version of this figure is available in the online journal.)

$$\partial_t \tau + \partial_j (r^2 \sin \theta T^{0j} - \rho_* v^j) = -r^2 \sin \theta T^{0i} \psi_{,i}, \quad (5)$$

$$\partial_t (\rho_* A) + \partial_j (\rho_* A v^j) = 0, \quad (6)$$

$$\Delta \psi = 4\pi \rho_0 \left[ 2h(u^t)^2 - h + 2 \frac{p}{\rho_0} \right], \quad (7)$$

where the subscript  $j$  runs over  $r$  and  $\theta$ , and  $A$ ,  $T^{\mu\nu}$ ,  $u^\mu$ , and  $\psi$  denote the mean molecular weight, energy-momentum tensor of ideal fluid, four-velocity of matter, and gravitational potential, respectively, and

$$\rho_* \equiv r^2 \sin \theta \rho_0 u^t, \quad (8)$$

$$S_i \equiv r^2 \sin \theta T^0_i, \quad (9)$$

$$\tau \equiv r^2 \sin \theta T^{00} - \rho_*. \quad (10)$$

The above equations are derived from the Einstein equations and energy-momentum conservation equations by the weak-field approximation, ignoring the time derivative of gravitational potential and space derivatives of three-dimensional space metric. Since our computational domains do not contain the origin, the gravity of the central object is added as a point mass at the center. The time evolution of the mass of the central object is taken into account by integrating the mass flux crossing the inner boundary of the computational domain.

We solve the Poisson equation for the gravitational potential, Equation (7), by MICCG and the hydrodynamical equations, Equations (1)–(6), by the central scheme (Kurganov & Tadmor 2000; Nagakura & Yamada 2008). In the latter, using the piecewise parabolic method (PPM) interpolation method and the total variation diminishing (TVD) Runge–Kutta time integration, we achieve second-order accuracy in both space and time.

The EOSs employed in this paper are the following. For Steps 2 and 3, that is, the construction of the stellar wind and the computation of the envelope collapse, the EOS by Blinnikov et al. (1996) is used, in which the temperature and mean molecular weight are introduced to avoid inconsistency with Step 1, where they are also accounted for. On the other hand, the so-called  $\gamma$ -law EOS,  $p = (\gamma - 1)\rho_0 \epsilon$ , with  $p$ ,  $\gamma = 4/3$ ,  $\rho_0$ , and  $\epsilon$  being the pressure, adiabatic index, rest-mass density, and specific internal energy, respectively, is adopted for the jet simulations in Step 4 for simplicity. Since we find that the envelope is radiation dominated at the time of jet launch, this is a good approximation.

It is a consensus that high-resolution simulations are necessary for the investigation of interactions between the jet and stellar envelope in the jet-drilling phase, since the Kelvin–Helmholtz instability and turbulent motions inevitably take place. When the velocity of the jet head is smaller than the local sound speed at the hot spot, which is indeed the case for the jet propagations in the stellar envelope, a back flow is bent and pinches the jet path (Mizuta et al. 2010a). In order to treat these effects adequately, we employ an adaptive mesh refinement (AMR) technique, in which the forward shock is searched at each time step and the number of mesh points in its vicinity is increased in each coordinate direction.

In the Appendix, we show the results of several numerical tests meant to validate our hydrodynamics code used in this paper. We also demonstrate that the rotational massive stellar envelope, which is constructed by the HSCF scheme at Step 1, does not change the configurations in a dynamic simulation, which is clear evidence that both codes are reliable.

### 2.3. A Quasi-steady Wind

Massive stars experience mass losses in general, and the GRB progenitors are not exceptions (Campana et al. 2006;

Soderberg et al. 2008). We hence take into account the stellar wind in our initial model (Step 2). It is noted, however, that theoretical understanding of the driving mechanism of stellar winds and mass losses of massive stars is far from satisfactory, and addressing these issues is much beyond the scope of this paper. We are, therefore, satisfied with the construction of quasi-steady winds without specifying its driving mechanism. What is important here is that the wind thus obtained does not change its configuration very much before the jet reaches it.

We first construct a spherically symmetric, steady wind configuration, neglecting rotation. For this purpose, we perform a one-dimensional (1D) hydrodynamic simulation, using the code described above, in the region from the stellar surface up to the distance of  $10^{13}$  cm. The initial configuration is rather arbitrary. Fixing the density, pressure, and velocity (or mass loss rate) at the inner boundary, we run a long-term simulation until the wind has settled to a steady state. The values of the density and pressure are chosen so that they will be continuous when the wind is appended to the envelope model constructed in Step 1. Rotation is then added so that the specific angular momentum should be constant along each radial ray. The values of the specific angular momentum at the inner boundary are chosen in such a way that they should be continuous from the envelope to the wind. The wind obtained in this way is not exactly steady anymore. Although rotational, steady wind configurations could be obtained in a similar way, it turns out that the wind configuration does not change much during the jet propagation through the envelope and wind if rotation is added this way. We hence do not pursue further elaboration in this paper.

By changing the inner boundary condition, we can construct various wind models, both dense and tenuous. In this paper, however, we adopt only an optically thin model to elucidate the effects of envelope motions on the jet dynamics. Other wind models and their influences on jet propagation will be investigated in the sequel to this paper (H. Nagakura 2011, in preparation). The photosphere of the present wind model is located at the stellar surface and the mass loss rate is  $\dot{M} \sim 10^{-6} M_{\odot} \text{ yr}^{-1}$ . Figure 3 shows the profiles of our wind model. The density and pressure distributions nearly obey power laws with the power-law indices being approximately  $-2.14$  and  $-2.82$ , respectively. The outflow in the wind becomes supersonic at  $r \sim 7.5 \times 10^{10}$  cm and its velocity asymptotically approaches  $v_{\text{asym}}^r \sim 2 \times 10^8 \text{ cm s}^{-1}$ .

#### 2.4. Collapse of the Massive Star Envelope

Using the envelope and wind configurations obtained above as an initial condition, we perform 2D axisymmetric simulations of the envelope collapse (Step 3). The computational domain covers at first a region of  $5 \times 10^6 \text{ cm} < r < 2 \times 10^{12} \text{ cm}$ , which includes the entire envelope and the core region except the black hole and its close vicinity, as well as the inner part of the wind. The inner boundary is shifted outward later (see below). The radial grid consisting of 224 points is not uniform, with the grid width changing with the density scale height. The angular grid covers a quadrant of the meridian section and is uniform with 60 points.

In reality, as we mentioned earlier, the gravitational collapse of the envelope is initiated by the arrival of the rarefaction wave that is generated at the core/envelope boundary by core collapse and propagates outward. To mimic this, we reduce the radial gradients of all quantities to zero at the inner boundary and artificially induce the infall there. Then a rarefaction wave

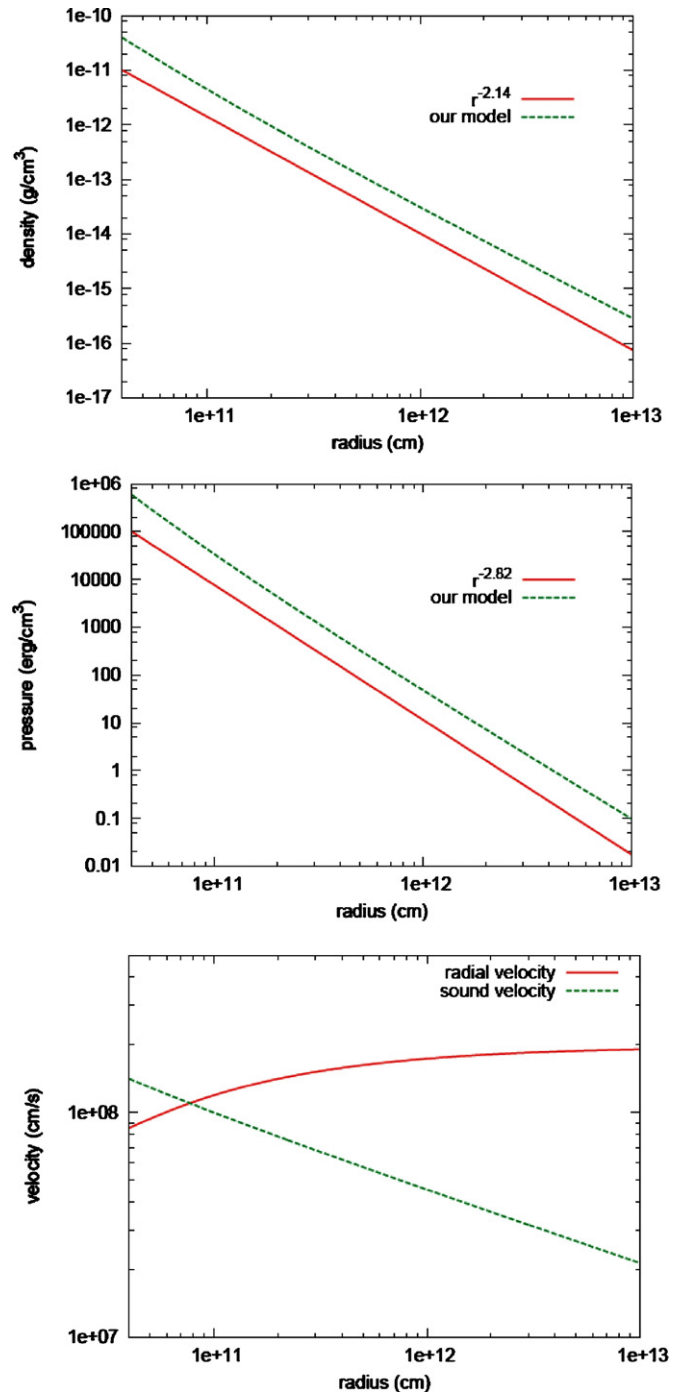


**Figure 3.** Profiles of density (top panel), pressure (middle panel), and radial velocity as well as sound velocity (bottom panel) for the wind model employed in this paper. The red lines in the top and middle panels show power laws for comparison. As shown in the bottom panel, although the radial velocity is initially subsonic, it passes a sonic surface, which is located at  $r \sim 7.5 \times 10^{10}$  cm. (A color version of this figure is available in the online journal.)

is produced at the inner boundary and propagates outward, inducing infall at points it reaches. It is stressed that we confirmed by the test computation presented in Appendix A.6 that if we do not reduce the radial gradients of quantities at the inner boundary, the envelope remains intact even after many time steps.

As shown in the next section, the contraction of the envelope is eventually terminated by centrifugal forces, producing a shock



wave that propagates outward and eventually breaks out of the stellar envelope. We increase the number of radial grid points to 1000 at the time of the shock breakout and shift the inner boundary outward to  $5 \times 10^8$  cm simultaneously. All the quantities are linearly interpolated to the new mesh points. The change of the inner boundary leads to the increase of the mass of the central object, which is properly taken into account, whereas we discard the angular momentum and energy between the old and new inner boundaries only for simplicity.

It should be noted that our numerical code does not take into account general relativity and detailed microphysics such as photodissociations of nuclei and neutrino cooling. The neglect of these effects tends to overestimate the strength of the shock wave of the centrifugal bounce origin. In fact, it was pointed out by Lindner et al. (2010) and Milosavljevic et al. (2010) that the nuclear photodissociations may completely sap the shock wave. We will defer the investigation of this issue to a future work, in which we will implement a nuclear network in our hydrodynamics code. We must repeat that we assume in this paper that the prompt shock wave of the core bounce origin is swallowed into the central black hole and what occurs inside it does not affect the dynamics of the envelope. In order to see if this assumption is correct or not, it is necessary to perform detailed simulations of core collapse in full general relativity, which is a major undertaking and will also be a future work.

### 2.5. Jet Injection and Propagations through the Stellar Envelope and Wind

In the next step (Step 4), which is the main part of this paper, we numerically study the jet propagations that are in motion through the stellar envelope and wind, as obtained in the previous step. Following common practice, we inject a relativistic jet from the inner boundary, not specifying the driving mechanism, at two different times after the envelope collapse takes place: 20 s for model M20s and 50 s for model M50s. The injection parameters are identical for both models: the jet is hot ( $p/\rho_0 c^2 = 20$ , where  $c$  is the speed of light) and relativistic with a Lorentz factor of five; the half-opening angle is  $9^\circ$ ; the power of the jet is constant in time, and the injection continues for  $t_{\text{dur}} = 30$  s with the total injected energy being  $10^{53}$  erg. Then the terminal Lorentz factor is estimated by

$$\begin{aligned} \Gamma_{\text{term}} &\equiv h_{\text{in}} \Gamma_{\text{in}} = (1 + \epsilon_{\text{in}} + p_{\text{in}}/(\rho_{\text{in}} c^2)) \Gamma_{\text{in}} \\ &\sim \gamma/(\gamma - 1) \times p_{\text{in}}/(\rho_{\text{in}} c^2) \times \Gamma_{\text{in}} \\ &= 4\{p_{\text{in}}/(\rho_{\text{in}} c^2)\} \Gamma_{\text{in}}, \end{aligned} \quad (11)$$

where  $h_{\text{in}}$ ,  $p_{\text{in}}$ ,  $\rho_{\text{in}}$ , and  $\Gamma_{\text{in}}$  are the specific enthalpy, pressure, rest-mass density, and Lorentz factor at the injection, respectively; the adiabatic index is denoted by  $\gamma$  and is set to be 4/3. The choice of the injection parameters in this paper corresponds to  $\Gamma_{\text{term}} \sim 400$ .

The computational domain for these simulations ranges from  $r = 10^9$  cm up to  $r = 10^{18}$  cm. Note that this broad range is mandatory for the identification of the locations of the photosphere until  $t_{\text{obs}} \sim 100$  s, since the forward shock in the jet is highly relativistic with a Lorentz factor of  $\Gamma > 100$ . The total number of radial grid points is 11,000. The grid is nonuniform, with the grid width being smallest ( $\Delta r = 10^8$  cm) at the inner boundary and increasing geometrically by  $\sim 0.1\%$  per zone up to  $10^{13}$  cm and by  $\sim 1.35\%$  in the region further out. The number of angular grid points, 60, is the same as in the previous step. We remap the data obtained in the previous step to the new grid by the same linear interpolation

as employed in Step 3. The shift of the inner boundary requires an adjustment of the mass of central objects, with the mass between  $5 \times 10^6$  ( $5 \times 10^8$ ) cm  $< r < 10^9$  cm being added to the central point mass for model M20s (M50s). The density, pressure, and velocity in the region of  $10^{13}$  cm to  $10^{18}$  cm are extrapolated from the inner region in the following manner: The density and pressure are extended by the power laws that fit their distributions in the inner region; the radial velocity is assumed to be constant in the extended region, since it has already reached the asymptotic velocity (see the bottom panel of Figure 3); and the  $\theta$  component of velocity is set to be 0, whereas the azimuthal component is determined so that the specific angular momentum is constant along each radial ray just as in Step 2.

During the jet propagation through the stellar envelope, we employ an AMR technique. In our code, there are only two levels of meshes deployed in which the resolution of the second level can be varied. Here the mesh of the second level is nine times finer than the first level mesh, with the smallest radial and angular resolutions being  $\Delta r = 1.1 \times 10^7$  cm and  $\Delta\theta = 0.16$ , respectively. After the jet breakout, on the other hand, the jet head expands nearly freely and soon becomes highly relativistic. As a result, the back flow tends to be suppressed and the jet morphology does not change much during this phase. We hence employ only three times finer a mesh for the second level after the jet head reaches  $R = 10^{11}$  cm. The resolution in this study is not as high as in the previous study (Lazzati et al. 2009). One of the main reasons for this is the fact that we are dealing with a much greater spatial extent. This is necessary, as already mentioned, in order to identify the locations of the photosphere. As a result, however, rapid variations in the photospheric emissions are sacrificed to some extent by numerical dissipations, and our discussions on this issue are restricted to a qualitative level.

### 2.6. Photospheric Emissions

As a final step (Step 5), we calculate, as a postprocess, the photospheric emissions based on the data obtained in Step 4. We define the photosphere to be the surface that has a unit optical depth from infinity with respect to the Thomson scattering. The optical depth is given by

$$\tau(t_{\text{obs}}, r) = \int_r^\infty n_e(t^*, s) \sigma_T \Gamma(t^*, s) (1 - \beta(t^*, s) \cos \theta_v(t^*, s)) ds, \quad (12)$$

where  $s$  is the distance along the line of sight,  $n_e$  is the number density of electrons in the comoving frame,  $\sigma_T$  is the cross section of the Thomson scattering,  $\beta$  is the matter velocity normalized by the speed of light  $c$ ,  $\Gamma$  is the corresponding bulk Lorentz factor, and  $\theta_v$  is the angle between the line of sight and the matter velocity (Abramowicz et al. 1991). It should be stressed that the time retardation expressed by  $t^* = t_{\text{obs}} - s/c$  in the above equation cannot be ignored for relativistic flows. In this paper, we evaluate Equation (12) as is, retrieving the data for appropriate times from the results of the hydrodynamic simulations. Thanks to the wide spatial range of our hydrodynamic simulations, photons observed at  $t_{\text{obs}} \lesssim 100$  s have passed the forward shock by the end of simulations, a fact which is important for the identification of the locations of the photosphere.

The observed isotropic luminosity of photospheric emissions is then given by

$$L = 4\pi \int \mathcal{D}^4 I \cos \theta_{\text{ph}} dS. \quad (13)$$

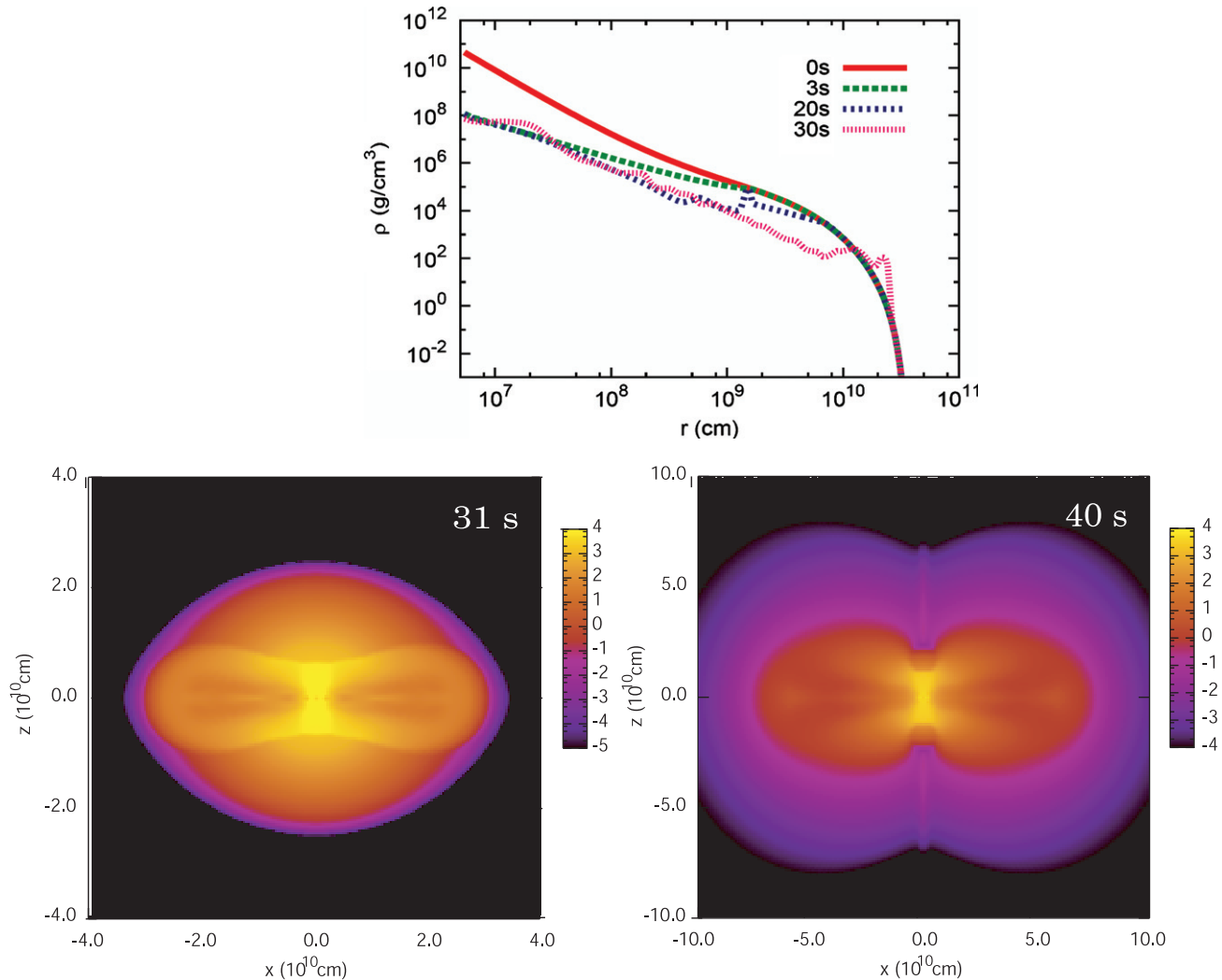


**Figure 4.** Time evolution of the density profile on the equator during the envelope collapse (top panel) and the density contours in the meridian section at the time of the breakout of the shock wave produced by centrifugal bounce (bottom left panel) and  $\sim 10$  s later (bottom right panel).

(A color version of this figure is available in the online journal.)

Here,  $dS$  is the areal element of the photosphere (measured in the laboratory frame),  $\mathcal{D} = [\Gamma(1 - \beta \cos \theta_v)]^{-1}$  is the Doppler factor,  $\theta_{\text{ph}}$  is the angle between the line of sight and the normal vector of the photosphere,  $I = \sigma_{\text{SB}} T^4 / \pi$  is the radiation intensity with  $\sigma_{\text{SB}}$ , and  $T$  is both the Stefan–Boltzmann’s constant and the temperature in the comoving frame. We ignore cosmological redshift in this study.

### 3. RESULTS

#### 3.1. Envelope Collapse

The top panel of Figure 4 shows the temporal evolution of the density profile on the equator obtained in Step 3, that is, the computation of envelope collapse. The infall starts at the inner boundary, generating a rarefaction wave that propagates outward. Only after this rarefaction wave arrives do other parts of the envelope begin to move inward. The contraction is initially almost spherical. As time passes and more distant portions of the envelope start to infall, however, the centrifugal force becomes non-negligible, since the specific angular momentum is an increasing function of radius. The centrifugal force eventually becomes large enough to halt the infall of matter, and a shock

wave is generated. This happens at  $t \sim 18$  s in our model. A similar but slightly later bounce by the centrifugal force was also reported by Lindner et al. (2010). The reason we found the earlier formation of the shock wave is that we put the inner boundary at a much smaller radius than Lindner et al. (2010). Indeed, the inner boundary of our model is initially located at  $\sim 3$  times the Schwarzschild radius, which is 10 times smaller than that adopted in Lindner et al. (2010). It should be noted that, as we have already mentioned, the shock wave is expected to be produced near the ISCO in reality and more accurate computation of its formation requires implementation of general relativity as well as microphysics such as neutrino transports and photodisintegrations of nuclei, which may sap the shock wave.

The shock wave propagates more vigorously along the equator than along the rotational axis and reaches the stellar surface on the equator at  $t \sim 31$  s (see the bottom left panel of Figure 4). Then the shock wave breaks out of the stellar surface and runs further through the wind (see the bottom right panel of Figure 4). If the jet is launched earlier than the shock formation, the shock dynamics just described will be modified by the jet propagation. If the opposite is true, that is, the jet launch is later than the shock formation, the jet dynamics will

be affected by the shock propagation. In particular, if the jet launch is sufficiently delayed, the jet propagation in the wind and, as a result, the photospheric emissions, will be severely changed. Model M20s is meant for the former case, whereas the latter case corresponds to model M50s. Incidentally, the shock breakout in the latter case may account for the so-called precursor that is observed for some long GRBs. In fact, the typical time lag between the precursor and the prompt emission is several tens of seconds (Lazzati 2005), which is similar to what we find in our model. In this scenario, the high-energy emissions in the precursor are supposed to be similar to those in the shock breakout of ordinary supernovae (Falk 1978; Klein & Chevalier 1978; Matzner & McKee 1999; Waxman et al. 2007; Soderberg et al. 2008). More quantitative arguments for the precursor emissions from these shock waves are currently being undertaken (H. Nagakura et al. 2011, in preparation).

Incidentally, we assume in this paper that it is not the centrifugal-bounce-originated shock wave but something else that is responsible for the jet launch. We hence treat the centrifugal bounce and the jet launch as independent events and rather freely vary the time of jet injection with respect to the centrifugal bounce. In reality, they may be correlated with each other one way or another. As we have already mentioned, the focus in this paper is the consequences that the possible time lag between these two events may have. The origin of the lag is intimately related to the mechanism of the jet launch. Although it is very interesting in its own right, the issue is far beyond the scope of this paper.

### 3.2. Jet Propagations in the Stellar Envelope and Wind

As expected, the hydrodynamics of the early injection model M20s (see the left column of Figure 5) is similar to those found in the previous studies (Lazzati et al. 2009; Mizuta et al. 2010b), since the envelope bounce by the centrifugal force occurs almost at the same time as the jet launch and the outer envelope structure has not been changed very much from the initial one. The jet is strongly collimated by a hot cocoon, i.e., the shocked jet and envelope matter, until the jet breaks out of the progenitor surface. Then the shocked jet matter starts to expand laterally from the vicinity of rotation axis and the internal energy is gradually converted to kinetic energy. As a result, the hot, shocked jet matter acquires a high Lorentz factor and produces very bright photospheric emissions (see the next subsection). Since the jet injection is terminated at  $t = 30$  s in this model, a rarefaction wave is generated at that point and starts to chase the jet head; only the matter between the jet head and rarefaction wave contributes to subsequent radiations.

For model M50s, in which the jet is launched much later than the envelope bounce, the jet dynamics are very different from the one for the early injection case (see the right column of Figure 5). The jet propagates through the envelope, which is not contracting but expanding owing to the shock wave produced at the centrifugal bounce of envelope. We find that the distance between the terminal (reverse) and forward shocks is shorter than for model M20s and the terminal shock remains in existence much longer for model M50s. The forward shock region in the jet is also found to be remarkably different after the breakout between the two models. Since the shock wave breaks out of the star before the relativistic jet reaches the stellar surface, the stellar wind is modified substantially by the shocked envelope matter (SEM). As a consequence, the jet propagation is hindered by the thick SEM even after it passes the position of the original stellar surface. The forward shock velocity becomes slower until

a much later time when the jet passes completely through the SEM, producing a denser shell behind the forward shock (see the second panel in the right column of Figure 5). This has important ramifications for the photospheric emissions later on.

### 3.3. Photospheric Emissions

In Figure 6, we display the light curves together with the evolutions of photospheric radii and observed temperatures ( $DT$ ) for both models. The observer is assumed to be located on the rotational axis (on-axis observer), and the photospheric radius in the figure is the value on the axis although we do calculate the positions of photosphere for off-axis rays. For model M20s, the luminosity peaks in an early phase ( $t_{\text{obs}} \lesssim 10$  s) and rather high luminosities are sustained for the next 30 s, whereas a strong peak is observed at a later time ( $t_{\text{obs}} \sim 25$  s) for model M50s. As already mentioned, this difference arises from the large difference in the envelope structures prior to the jet breakout. Since a larger amount of matter is swept up by the jet in model M50s, it takes the photosphere longer to leave the forward shock region and move inward to a region with higher observed temperatures, producing bright radiations. This qualitative difference in the light curves may be utilized to observationally extract information on the timing of jet launch at the central engine.

As an explanation of the GRB prompt emissions, the photospheric emissions in our models have sufficiently high luminosities. The peak energy, however, is lower by roughly an order of magnitude than the value expected from the Yonetoku relation (Yonetoku et al. 2004). This tendency is the main drawback of the photospheric emission model. Note, however, that the shocked jet matter may be scattering dominant and energy exchanges between photons and matter may be terminated deeper inside. If this is the case, the observed temperatures will be higher and the luminosity will also be reduced. The study of these effects is currently in progress (H. Ito et al. 2011, in preparation). It is also conceivable that some non-thermal processes are operating to produce high energy photons. Further exploration of these issues will require detailed computations of radiation transport and will also be a future work.

## 4. SUMMARY

We have numerically investigated the propagations through a rapidly rotating massive star envelope of relativistic jets that are launched at different times, taking into account the motions of the envelope induced by core collapse. Then, we have calculated the photospheric emissions by postprocessing. The main findings in this paper are summarized as follows.

1. In the envelope collapse, we have seen the generation of a shock wave by the centrifugal force around  $t \sim 20$  s for the progenitor rotating uniformly at the mass shedding limit. In  $\sim 10$  s, the shock wave breaks out of the star if the jet launch is sufficiently delayed.
2. If the shock wave produced by the centrifugal force breaks out of the star earlier than the jet does, it changes the envelope and wind structures drastically and the jet propagation thereafter is also significantly affected. In fact, in that case, since the forward shock in the jet sweeps up a larger amount of matter, a dense shell is produced behind it.
3. The light curve of photospheric emissions is qualitatively different if the jet is launched later and propagates in the shock-modified envelope and wind. In the case of earlier launch, peak luminosity is attained at a relatively early time

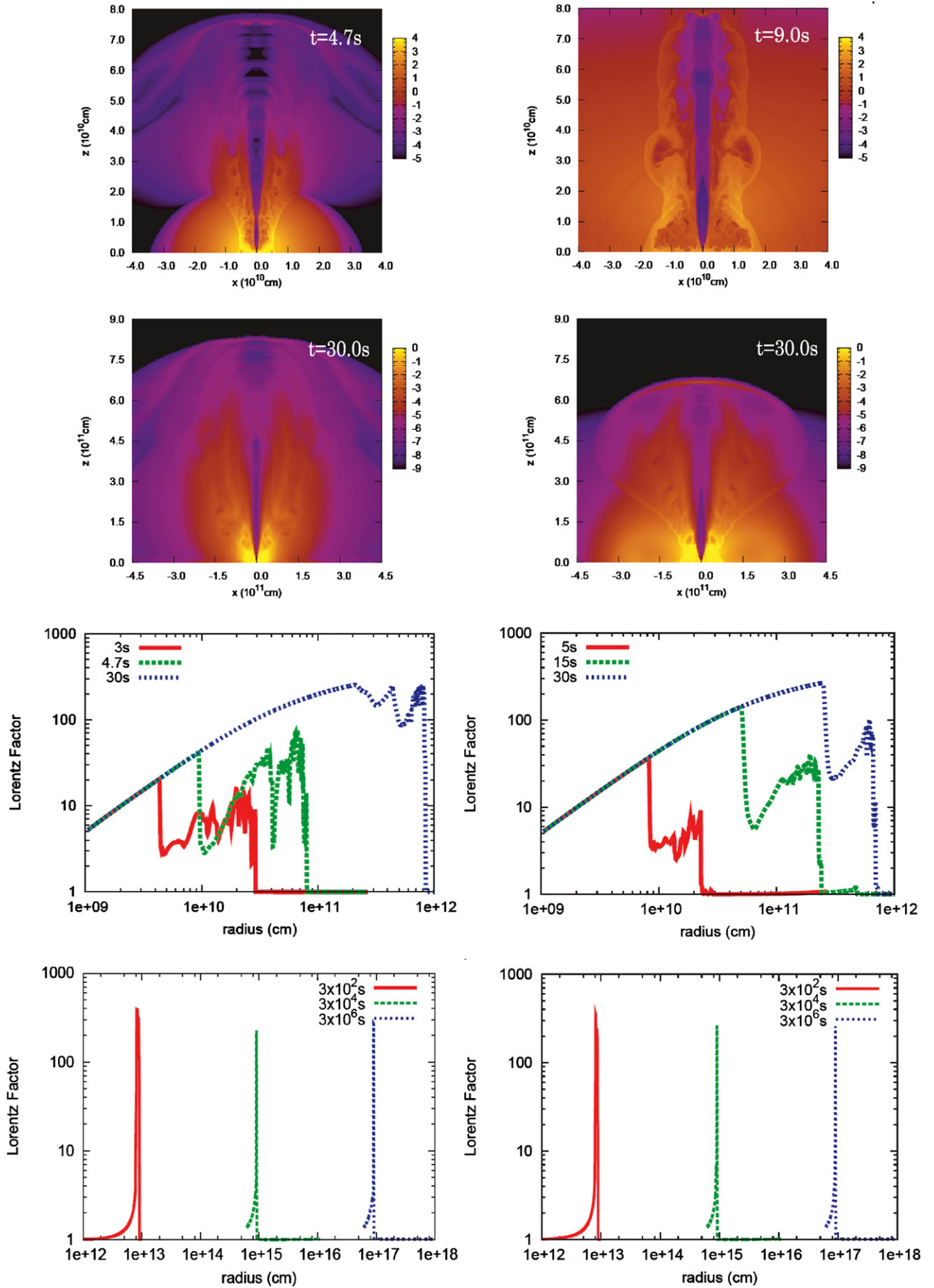


**Figure 5.** Density contours (upper four panels) and time evolutions of the Lorentz factors on the rotational axis (lower four panels) for model M20s (left column) and model M50s (right column). The time,  $t$ , is measured from the instant at which the jet is injected.

(A color version of this figure is available in the online journal.)



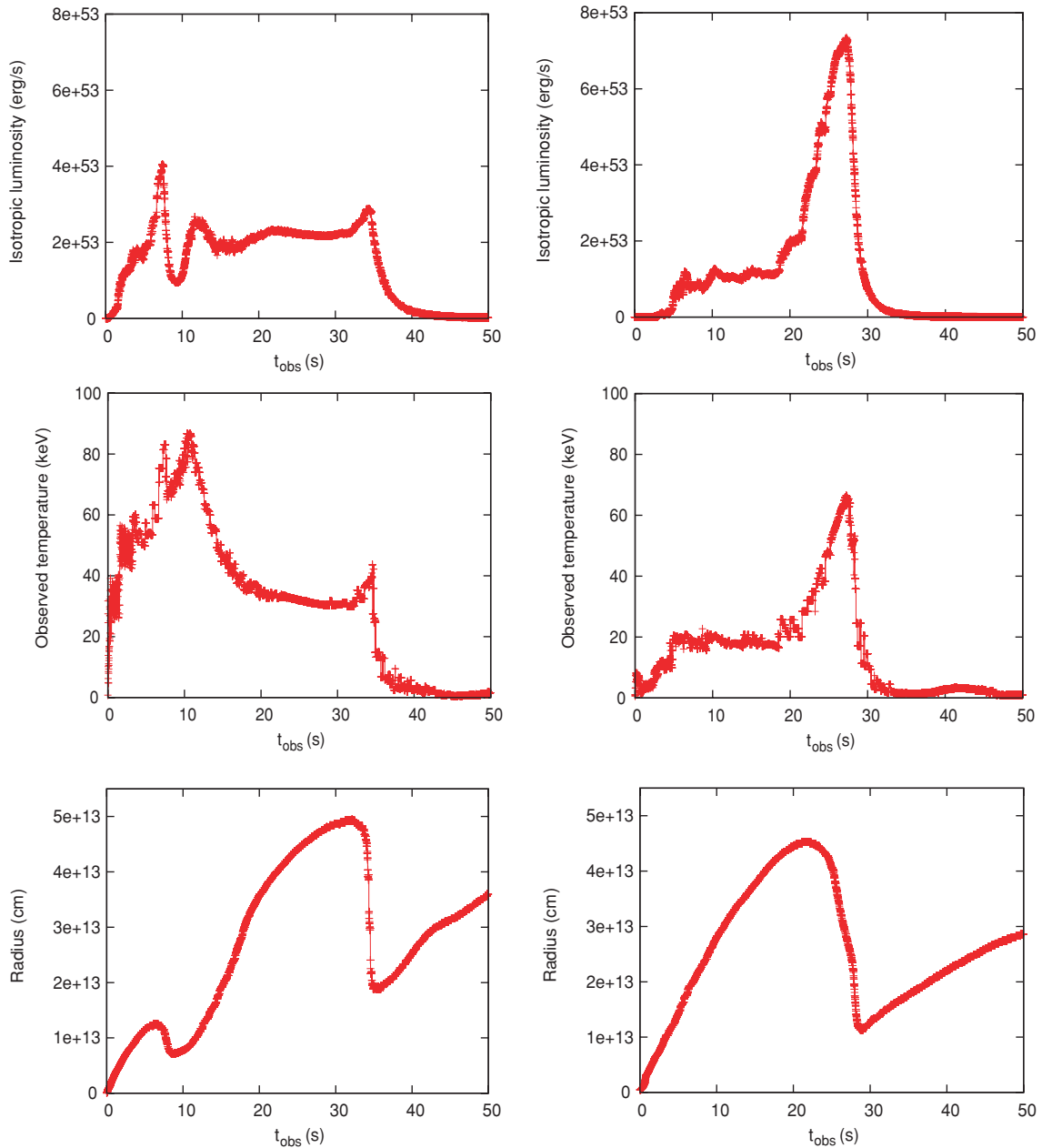


**Figure 6.** Light curves of photospheric emissions (top panels), evolutions of the observed temperature (middle panels) and of the photospheric radius (bottom panels) as a function of the observed time for model M20s (left column) and model M50s (right column). See the text for details.

(A color version of this figure is available in the online journal.)

( $t_{\text{obs}} \sim 10$  s), whereas it takes longer ( $t_{\text{obs}} \sim 25$  s) to observe the peak for the delayed launch case owing to the previously mentioned dense shell.

4. The photospheric emissions obtained in this study with time retardation taken into account appropriately have high luminosities suitable for the GRB prompt emissions. However, the peak energy tends to be lower than expected from the Yonetoku relation. If the shocked jet matter is scattering dominated, photons will cease to exchange energy with matter deeper inside, where the temperature is higher. It is also possible that some non-thermal processes boost the photon energy.

The light curves of our results are different from those given in previous papers (Lazzati et al. 2009; Mizuta et al. 2010a). Since the focus in this paper is to investigate possible

consequences that the difference in the timing of jet launch may have for the prompt emissions, we have not made detailed comparisons with these previous studies. There are, however, several conceivable causes for the differences: (1) better estimation of the location and temperature of photosphere thanks to the wider computational domain; (2) the effect of envelope collapse being taken into account; and (3) the differences in the jet-injection parameters, progenitor models, and numerical resolutions. These issues will be addressed in our forthcoming paper.

We thank Akira Mizuta and Shigehiro Nagataki for useful discussions. This work is partially supported by the Japan Society for Promotion of Science (JSPS) Research Fellowships, Grant-in-Aid for the Scientific Research from the Ministry of Education, Culture, Sports, Science and Technology, Japan

(Nos. 222913, 22740178, 21540281, 19104006). This study is also supported by the Program for Improvement of Research Environment for Young Researchers from Special Coordination Funds for Promoting Science and Technology (SCF), commissioned by the Ministry of Education, Culture, Sports, Science and Technology (MEXT) of Japan.

## APPENDIX CODE TESTS

In this appendix, we carry out a series of tests in order to validate our special relativistic hydrodynamics code, which employs the PPM reconstruction and TVD Runge–Kutta integration with second-order accuracy in both space and time. We adopt a Harten–Lax–van Lee (HLL)-type numerical flux and the Courant–Friedrichs–Lewy (CFL) number is set to be 0.5. Included in the following are: (1) 1D special relativistic shock tube problems, (2) the same as (1) but with tangential velocities, and (3) a 2D Riemann problem. The 1D problems are compared with the exact solutions, and we utilize the results given in previous papers for the 2D problem. We also solve (4) 1D and (5) 2D isentropic flows to quantitatively obtain the convergence rate. For these test runs (1)–(5), the  $\gamma$ -law EOS is adopted with the adiabatic index of  $\gamma = 5/3$ . We also run (6) a dynamic simulation of the rotating stellar envelope, which is obtained by the HSCF method (see Section 2.1) and confirm that the stellar envelope sustains the initial profile for an extended time. In order to check the accuracy of our AMR part, we compute (7) a non-relativistic, spherical point explosion, which can be compared with the Sedov–Taylor analytical solution; (8) a pulse propagating adiabatically through meshes of different refinement levels; and (9) an axisymmetric, relativistic jet propagation in a uniform matter. These tests demonstrate that our numerical code has enough accuracy for the purpose of the current study. Throughout this appendix, we adopt geometrical units  $G = c = 1$  unless otherwise stated.

### A.1. 1D Relativistic Shock Tube Problems without Tangential Velocities

The shock tube problem is one of the common tests for hydrodynamic codes. It is a special Riemann problem in gas dynamics. One of the advantages of this test is the fact that we know exact solutions even in special relativity (Pons et al. 2000). We can check how well the code reproduces the profile of a rarefaction wave and captures several discontinuities such as contact surface and shock wave. In this test, we set the number of grid points to 400 and the parameters employed for two runs are as follows:

- Case 1. Left state:  $(\rho, v, p)^L = (10, 0, 13.3)$ ,  
Right state:  $(\rho, v, p)^R = (1, 0, 10^{-6})$
- Case 2. Left state:  $(\rho, v, p)^L = (1, 0, 10^3)$ ,  
Right state:  $(\rho, v, p)^R = (1, 0, 10^{-2})$ .

Figure 7 shows the results at  $t = 0.4$  together with the exact solutions. As is obvious, the overall profiles are reproduced well. Although the contact surface and shock wave are somewhat smeared out, our results are quite similar to those of other groups (see, e.g., Del Zanna & Bucciantini 2002).

### A.2. 1D Relativistic Shock Tube Problems with Tangential Velocities

Here we show the results of relativistic shock tube problems with tangential velocities. In the special relativistic shock tube

problems, the velocity components tangential to a discontinuity play a non-trivial role, unlike in the non-relativistic counterpart, because the Lorentz factor depends on the absolute value of the velocity and it is numerically harder to resolve the flow profiles in special relativity as reported by Pons et al. (2000) and Rezzolla & Zanotti (2002). In these tests, we adopt the same initial condition as in Case 2 of the previous subsection except for the non-vanishing tangential velocities, which are identical to those in Mizuta et al. (2006).

Figure 8 shows the results of these tests. We vary the tangential velocity  $v_y$  from 0 to 0.99 on both sides. It is clear that both the contact surface and shock wave are substantially deviated from the exact solutions as the tangential velocity becomes large. We perform test runs for  $(v_y^L, v_y^R) = (0.9, 0.9)$  with higher spatial resolutions (the number of grid points changes from 800 to 6400) and display the results in Figure 9. Although the deviations of the numerical results from the exact solution are still noticeable even in these high-resolution runs, we can confirm the convergence of the numerical results to the exact solution. Again the performance of our code is similar to others (see, e.g., Mizuta et al. 2006; Zhang & MacFadyen 2006).

### A.3. A 2D Riemann Problem

This test is meant to check the performance of our code in multi-dimensional settings. The computational domain is initially divided into four sections that have different states. The solution consists of multiple shock waves, contact surfaces, and a rarefaction wave interacting with each other. The parameters we adopt in this test are the same as in Del Zanna & Bucciantini (2002), Mizuta et al. (2006), and Morsony et al. (2007):

$$(\rho, v_x, v_y, p) = (0.1, 0.00, 0.00, 0.01) \\ \text{for } 0.5 \geq x \geq 1, 0.5 \geq y \geq 1$$

$$(\rho, v_x, v_y, p) = (0.1, 0.99, 0.00, 1.00) \\ \text{for } 0 \geq x \geq 0.5, 0.5 \geq y \geq 1$$

$$(\rho, v_x, v_y, p) = (0.5, 0.00, 0.00, 1.00) \\ \text{for } 0 \geq x \geq 0.5, 0 \geq y \geq 0.5$$

$$(\rho, v_x, v_y, p) = (0.1, 0.00, 0.99, 1.00) \\ \text{for } 0.5 \geq x \geq 1, 0 \geq y \geq 0.5.$$

We use a uniform mesh with  $400 \times 400$  grid points. Figure 10 shows a contour in the logarithm scale of the rest-mass density obtained in this simulation. There is no exact solution available. The results appear very similar to the ones presented in previous studies.

### A.4. A 1D Isentropic Flow

All the above tests involve discontinuities such as the shock wave. As a result, the code affords only a first-order accuracy because the numerical error is dominated by these structures. Note that this is necessary to ensure numerical robustness. In order to see the performance of our code for smooth flows, we carry out numerical simulations of 1D and 2D (see the next subsection) isentropic flows. The exact solutions are obtained by the characteristic method. Hence, the test offers an opportunity to quantitatively assess the accuracy of our code.

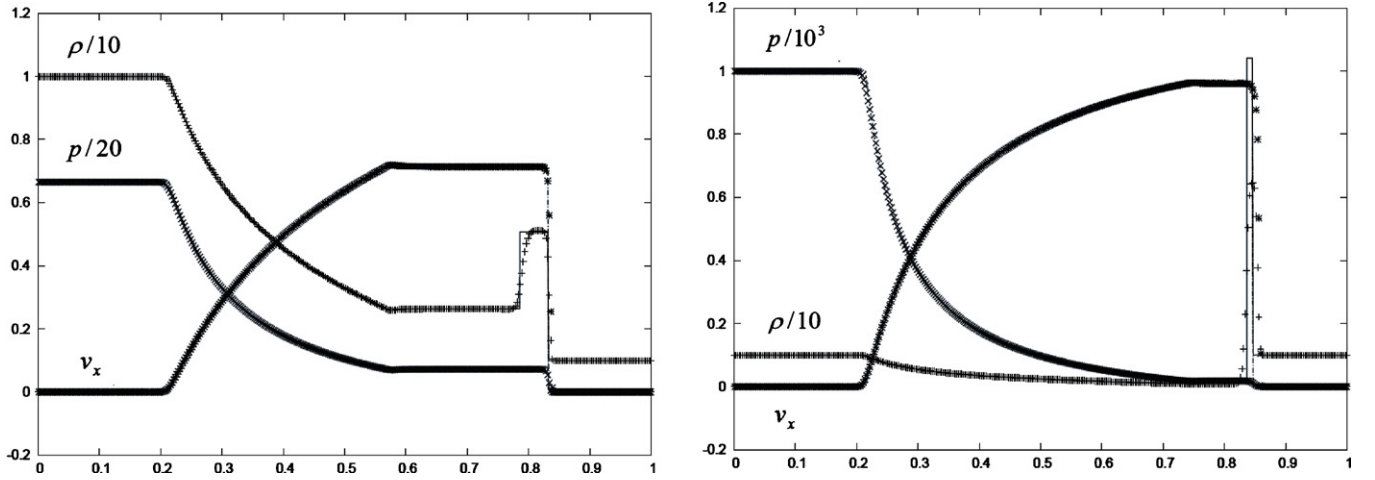


**Figure 7.** Numerical results (dots) for the 1D relativistic shock tube problems without tangential velocities. The rest-mass density ( $\rho$ ), pressure  $p$ , and velocity  $v_x$  are shown. The exact solutions (solid lines) are also displayed for comparison. The left (right) panel corresponds to case 1 (case 2) at  $t = 0.4$  ( $t = 0.35$ ).

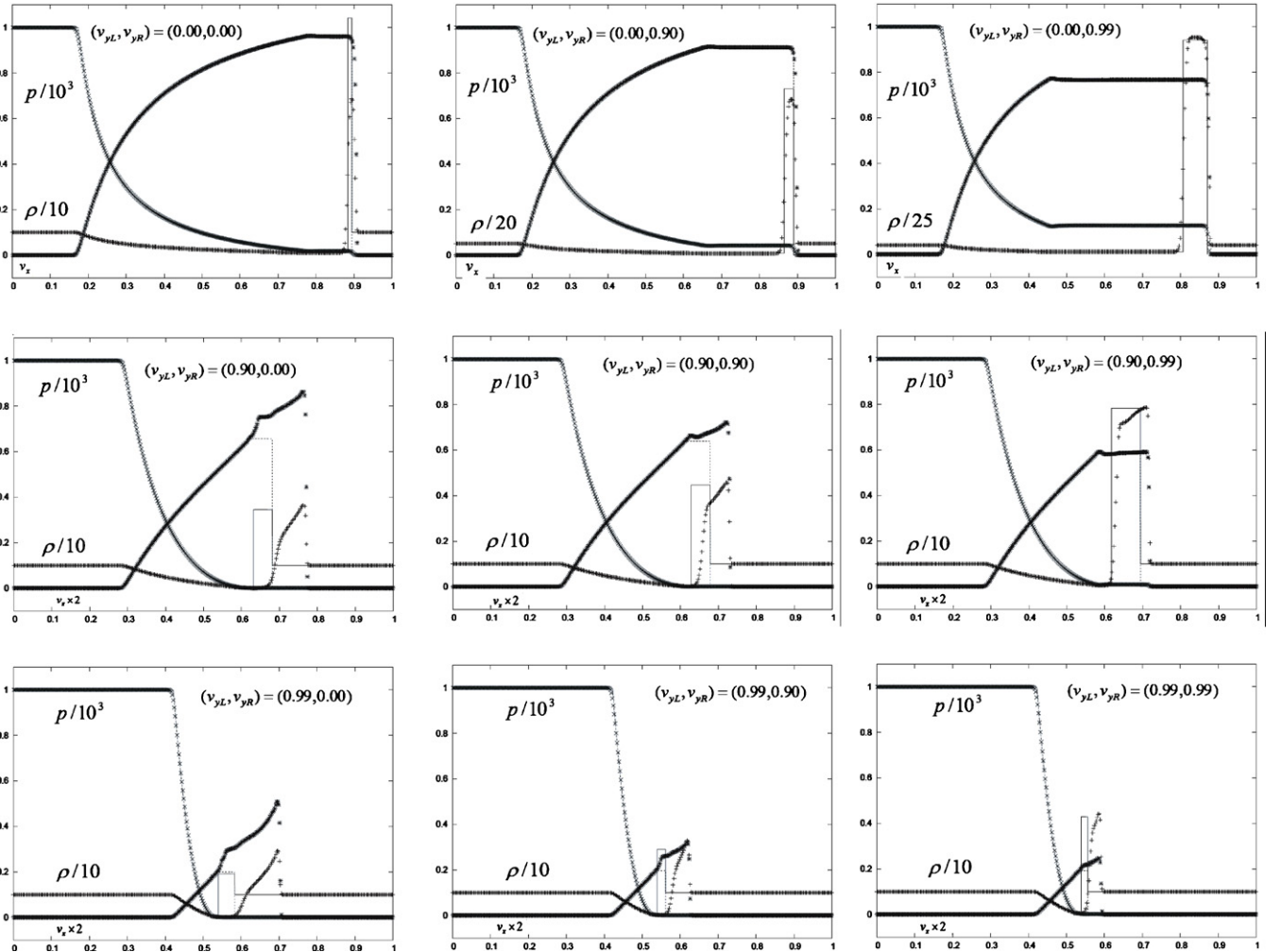


**Figure 8.** Numerical results (dots) for the 1D relativistic shock tube problems with tangential velocities. A uniform mesh with 400 grid points is employed. The exact solutions (solid lines) are also displayed for comparison. We change  $v_x^R$  from left to right as  $v_x^R = 0, 0.9, 0.99$  and  $v_y^L$  from top to bottom as  $v_y^L = 0, 0.9, 0.99$ . The density, pressure, and  $x$ -component of velocity are shown. See Figure 15 in Mizuta et al. (2006) for comparison.

The initial conditions for this test are the same as those employed in the previous studies (Zhang & MacFadyen 2006; Morsony et al. 2007), and the density profile is given by

$$\rho_0(x) = \rho_{\text{ref}}\{1 + \alpha f(x)\}, \quad (\text{A1})$$

where  $\rho_{\text{ref}}$  is the density of a reference state and

$$f(x) = \begin{cases} ((x/L)^2 - 1)^4 & : |x| < L \\ 0 & : \text{otherwise,} \end{cases} \quad (\text{A2})$$

with  $\alpha$  and  $L$  being the amplitude and width of a pulse,

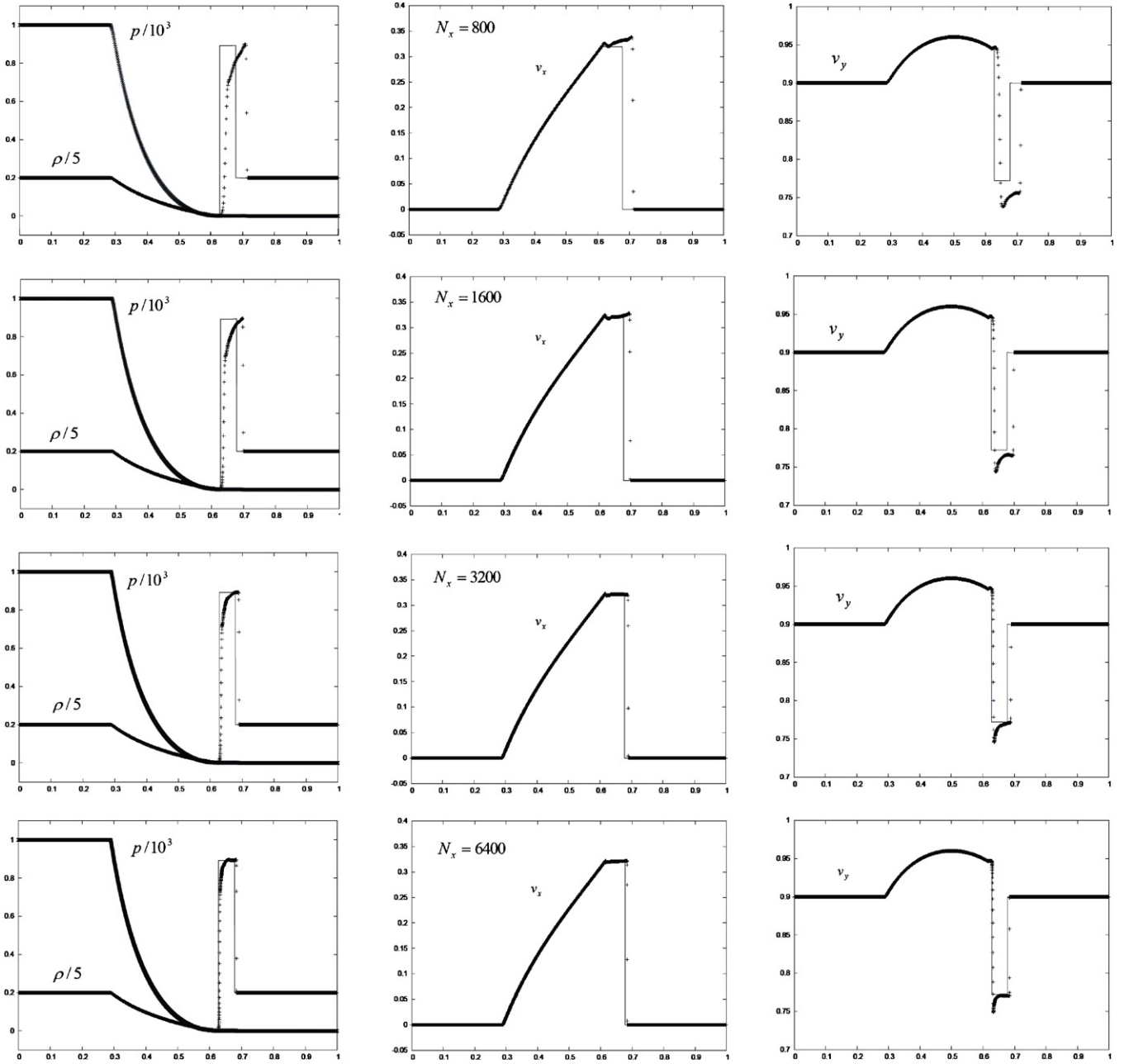


**Figure 9.** Numerical results (dots) for the same problem as in the previous figure ( $v_y^L, v_y^R$ ) = (0.9, 0.9) with different resolutions. These are meant to check the numerical convergence. The exact solutions (solid lines) are displayed for comparison. The left panels show the rest-mass density and pressure, whereas the middle (right) panels display the x-component (y-component) of velocity. From top to bottom, the numbers of grid points are 800, 1600, 3200, and 6400, respectively.

respectively. Since the flow is isentropic, we employ a polytropic EOS ( $p = K\rho_0^\gamma$ ) with the polytropic constant of  $K = 100$  and the adiabatic index of  $\gamma = 5/3$ . The velocity of the reference state is set to be 0, while the velocity distribution inside the pulse is chosen so that the left-going Riemann invariant should be constant. With this setup, the wave propagates in one direction. The special relativistic Riemann invariants are given by

$$J_{\pm} = \frac{1}{2} \ln \left( \frac{1+v}{1-v} \right) \pm \frac{1}{\sqrt{\Gamma-1}} \ln \left( \frac{\sqrt{\Gamma-1} + c_s}{\sqrt{\Gamma-1} - c_s} \right), \quad (\text{A3})$$

where  $c_s$  denotes the sound velocity. The equations of charac-

teristics  $C_{\pm}$  are expressed as

$$\left( \frac{dx}{dt} \right)_{C_{\pm}} = \frac{v \pm c_s}{1 \pm vc_s}. \quad (\text{A4})$$

Since the  $J_-$  and entropy are constant over the whole region, the pulse evolution is determined by the  $J_+$ , which is carried along the characteristic  $C_+$  until right-traveling characteristics collide with each other and a shock wave forms. Although the shape of the pulse is initially symmetric, it is skewed owing to different characteristic velocities. Note also that the post-pulse state is the reference state.

Our computational domain is the same as in previous studies (Zhang & MacFadyen 2006; Morsony et al. 2007): ( $-0.35 \leq x \leq 1$ ); the reference state has  $\rho_{\text{ref}} = 1$ ,  $p_{\text{ref}} = 100$ , and



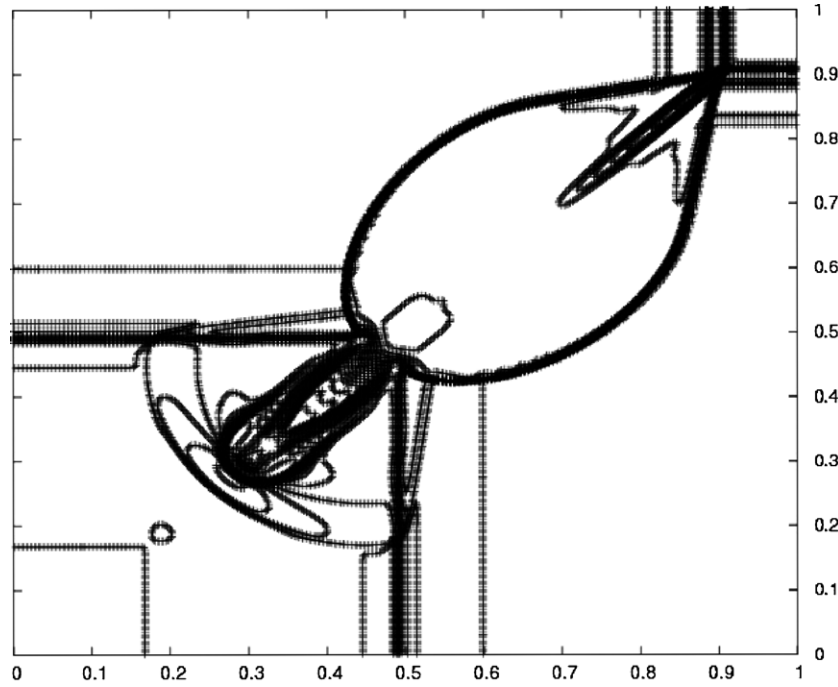


**Figure 10.** Contour plot of rest-mass density in the logarithmic scale at  $t = 0.4$  for the 2D Riemann problem.

**Table 1**

Numerical Errors for Different Resolutions in the 1D Isentropic-flow Problem

Number of Grid Points	$L^1$ Error (%)	Convergence Rate ( $\alpha$ )
100	0.58	...
200	0.17	1.83
400	3.67E-2	2.17
800	7.96E-3	2.20
1600	1.80E-3	2.14
3200	4.11E-4	2.13
6400	9.60E-5	2.10

**Notes.** The errors of density are evaluated at  $t = 0.8$ . In the rightmost column, the powers in the expression  $L^1 \propto N^{-\alpha}$ , where  $N$  denotes the number of grids, are given.

$v_{\text{ref}} = 0$ ; the amplitude of the pulse is  $\alpha = 1.0$ ; and the width is  $L = 0.3$ . The simulation is run until  $t = 0.8$ . A comparison of numerical and exact solutions is displayed in Figure 11. We also calculate the  $L^1$ -norm errors in density for different spatial resolutions, where  $L^1 \equiv \sum_j \Delta x_j |\rho_{0j} - \rho_0(x_j)|$ , with  $\rho_{0j}$  and  $\rho_0(x_j)$  being the numerical and exact solutions, respectively. In Table 1, we summarize the results of the convergence check for this problem. It is thus confirmed that our code indeed has a second-order convergence for smooth flows (see also Figure 12).

#### A.5. A 2D Isentropic Flow

We also perform a 2D computation of the isentropic flow to assess the convergence rate of our code in a multi-dimensional context. The initial condition for this test is the same as that in Zhang & MacFadyen (2006) and Morsony et al. (2007). The computational region is a 2D Cartesian box with  $0.0 \leq x \leq 3.75$  and  $0.0 \leq y \leq 5.0$ . The periodic boundary condition is adopted for all four sides of the box. The reference state is set to  $\rho_{\text{ref}} = 1$ ,  $p_{\text{ref}} = 100$ , and  $v_{\text{ref}} = 0$ . The polytropic EOS with the polytropic constant of  $K = 100$  and the adiabatic index of  $\gamma = 5/3$  is employed just as in the 1D case. Periodic

pulses are prepared initially in such a way that they have a spatial period of  $S = 3.0$  in the direction given by a unit vector,  $\mathbf{k} = (4/5, 3/5)$ , and are uniform in the perpendicular direction. The projected spatial periods in the  $x$ - and  $y$ -directions are 3.75 and 5.0, respectively, which is consistent with the size of our computational domain. The initial density profile is given by  $\rho_0(d)$  (Equations (A1) and (A2)), in which  $d$  is the distance from the center of the nearest pulse and expressed as  $d = \text{mod}(\mathbf{k} \cdot \mathbf{r} + S/2, S) - S/2$  with  $\text{mod}(a, b)$  being a function defined as  $\text{mod}(a, b) \equiv a - [a/b] \times b$ , where  $[a/b]$  denotes the integer part of  $a/b$ . The amplitude of the pulse is chosen to be  $\alpha = 1.0$  and the width is set to be  $L = 0.9$ . The velocity distribution in the pulse is determined as in the 1D case in the previous subsection so that  $J_-$  defined for this oblique 1D problem should be constant. The simulation is run up to  $t = 2.4$ .

Figure 13 shows the numerical result as a density contour at  $t = 2.4$ . In this figure, we display the case in which the numbers of grid points are set to be 96 and 128 in the  $x$ - and  $y$ -directions, respectively. As in the 1D counterpart, the pulse becomes asymmetric with the right side of the pulse becoming narrower than the left side. We also run some simulations with different numerical resolutions and confirm again that the convergence is approximately of second order (see Table 2 and Figure 14). Note that the error,  $\delta\rho_0$ , is defined as an  $L^1$  norm in 2D to be

$$\delta\rho_0 \equiv \frac{\Delta x \Delta y \sum_{j,k} |\rho_{0jk} - \rho_0(x_{j,k})|}{\Delta x \Delta y \sum_{j,k} \rho_0(x_{j,k})}, \quad (\text{A5})$$

where  $\rho_{0jk}$  and  $\rho_0(x_{j,k})$  are the numerical and exact solutions, respectively, for density at the mesh point having an address  $(j, k)$ .

#### A.6. Dynamic Simulations of Rotational Equilibrium

In order to check the consistency of the dynamic code with the code of the HSCF method employed to construct the rotational equilibrium, we run long-term simulations for the stellar

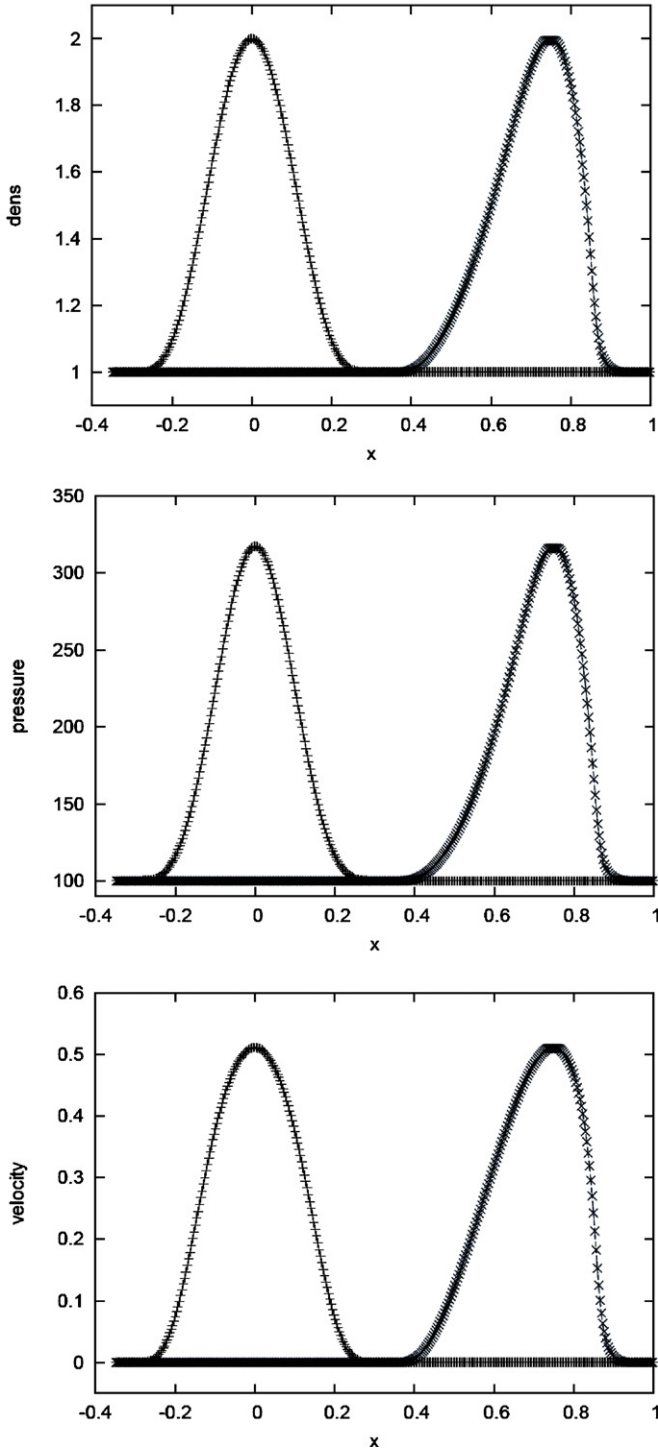


**Figure 11.** Initial ( $t = 0$ ) and simulated ( $t = 0.8$ ) density (top panel), pressure (middle panel), and velocity (bottom panel) profiles for the 1D isentropic flow together with the exact solution (solid lines). A uniform mesh with 400 grid points is employed.

envelope in rotational equilibrium, which is obtained by the HSCF method (see Section 2.1). The initial configuration will not change in time if it is indeed in dynamic equilibrium. The test will hence simultaneously validate both the hydrodynamics code with the weak gravitational field approximation and the HSCF code. The computations are essentially the same as those done in Step 3 in the main body except for a different treatment of the boundary condition. All the quantities are fixed at the

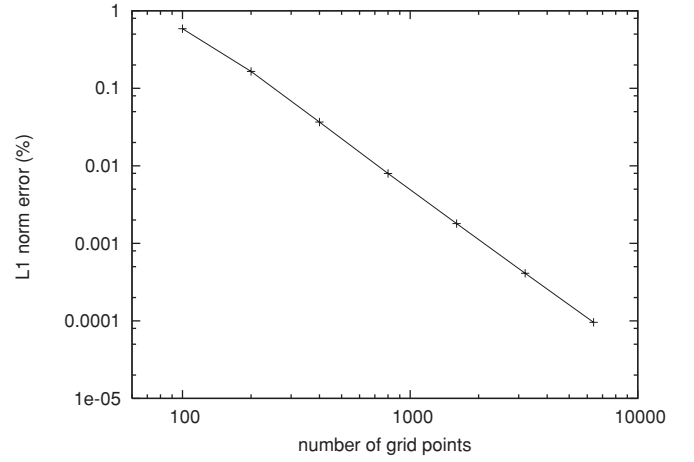


**Figure 12.**  $L^1$  density errors for the 1D isentropic flow as a function of the number of grid points.

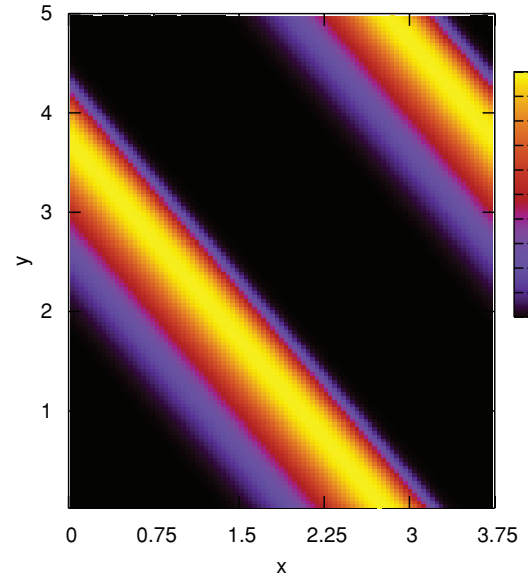


**Figure 13.** Numerical result of the density structure for the 2D isentropic-flow problem. The spatial resolution is effectively equivalent to the numbers of grid points of (96, 128) in the  $x$ - and  $y$ -directions.

(A color version of this figure is available in the online journal.)

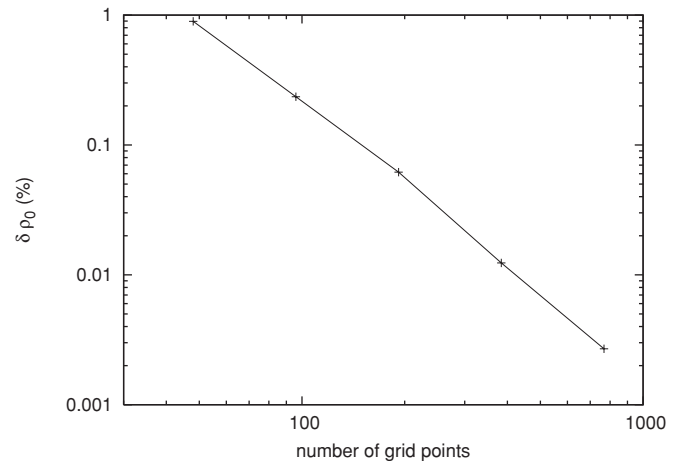


**Figure 14.** Density errors  $\delta\rho_0$  for the 2D isentropic flow as a function of the number of grid points.

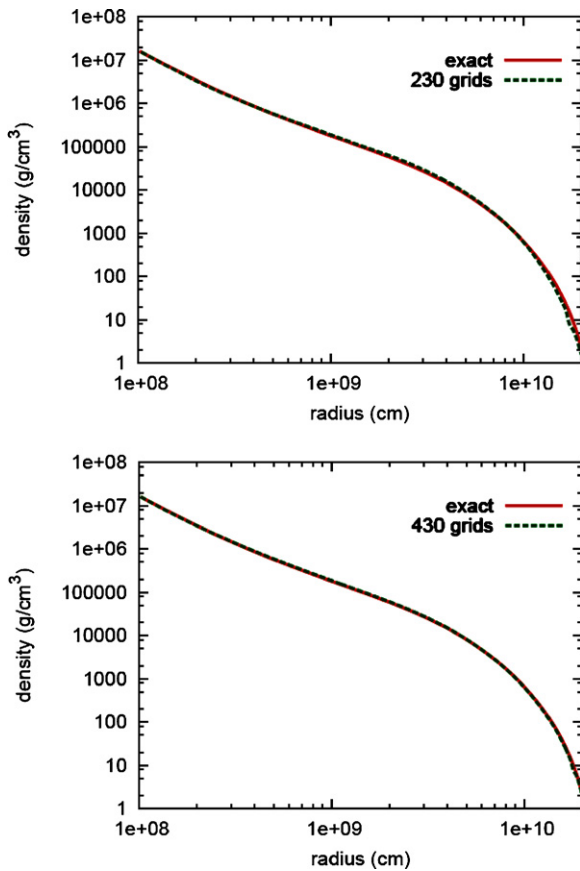


**Figure 15.** Density profiles along the rotational axis at  $t = 100$  s after the long-term dynamic simulations of the envelope in rotational equilibrium. Two spatial resolutions are employed with the top panel showing the result for 230 radial grid points (green line) together with the initial profile (red line), whereas the bottom panel corresponds to the result for 460 points.

(A color version of this figure is available in the online journal.)

boundaries to the values provided by the HSCF calculations, unlike in Step 3, where the radial gradients of the quantities are artificially reduced to zero. In this subsection, we adopt cgs units. The computational domain covers a radial extent of  $10^8 \text{ cm} < r < 2 \times 10^{10} \text{ cm}$ . The simulations are continued until  $t = 100$  s, which is much longer than the dynamic timescale in the inner region, where it is the shortest. Two spatial resolutions are tried to see the numerical convergence: the normal resolution with 230 radial points and the higher resolution with 460 points. Just as in Step 3, the grid width is determined by the scale height:  $\Delta r_{\text{in}} = 7.9 \times 10^6 \text{ cm}$  and  $\Delta r_{\text{out}} = 2.0 \times 10^8 \text{ cm}$  for the innermost and outermost grids, respectively, for the normal resolution, and they are two times finer for the high-resolution case. The angular grid is uniform and has 60 points in  $0^\circ < \theta < 90^\circ$ .

Figure 15 shows the density profiles along the rotational axis at the end of the simulations. The red lines are the profile obtained by the HSCF method and the green ones are numerical results. Deviations, which are inevitably induced by the mapping of the initial data as well as the difference in the finite-difference methods, are very small and it is indeed remarkable that the initial configuration is maintained for such a long time. This is clear evidence that both the hydrodynamics code and HSCF code are reliable. It should also be noted that these deviations are even smaller for the high-resolution case (see the bottom panel of Figure 15).

### A.7. Sedov–Taylor Problems

In order to validate our AMR implementation, we solve the Sedov–Taylor problem. Although our code is special relativistic, we use it in the non-relativistic regime here. It is also noted that, although the Sedov–Taylor problem is 1D, a 2D grid is employed for the computation since our AMR code used in this paper is specialized for the jet simulation and based on the axisymmetric, 2D grid.

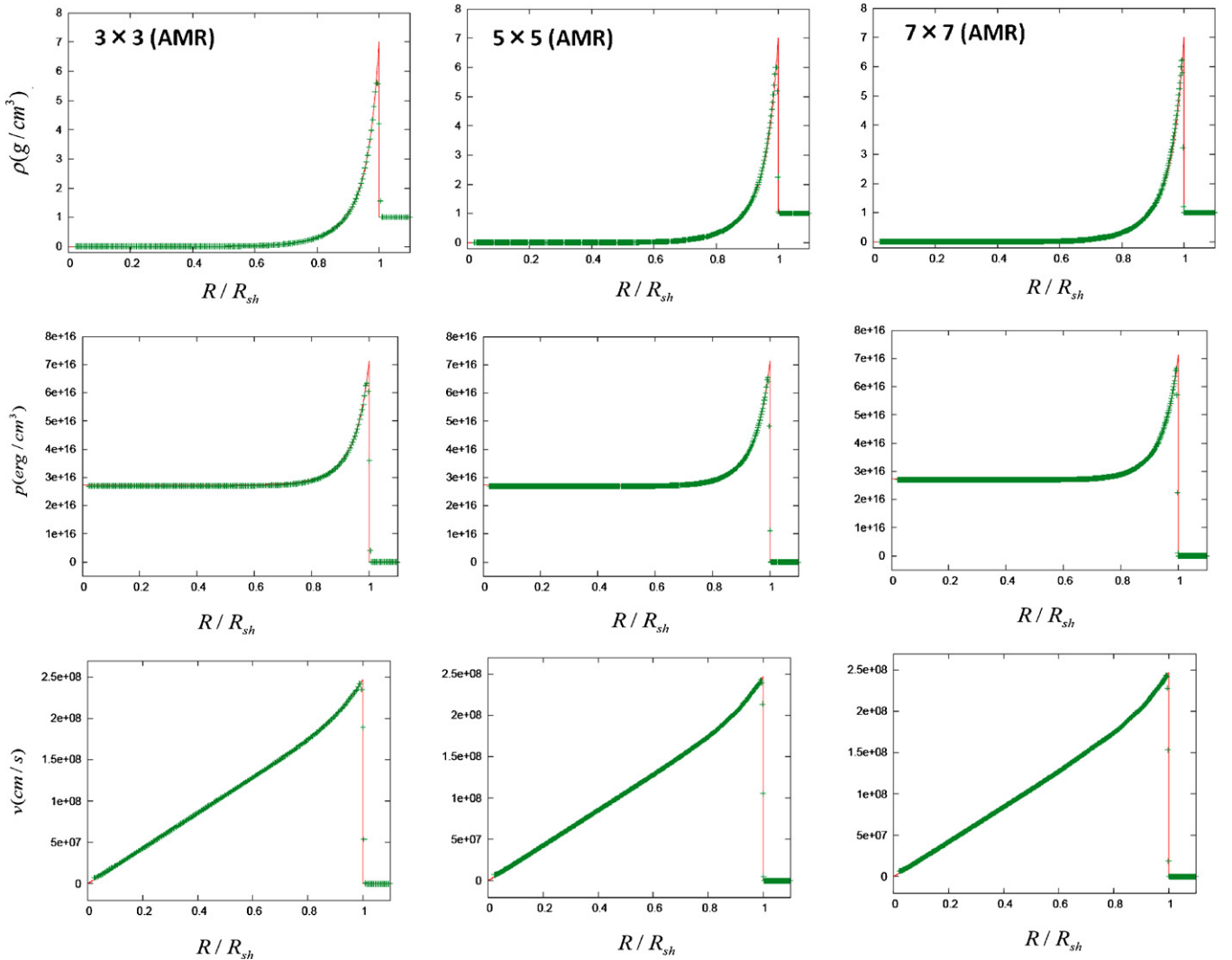
In this simulation, the computational domain,  $3 \times 10^8 \text{ cm} < r < 1.8 \times 10^{10} \text{ cm}$ , is covered by a uniform mesh with 100 radial grid points ( $\Delta r = 1.8 \times 10^8 \text{ cm}$ ) (this section is also adopted in cgs units). The internal energy of  $E = 1.60 \times 10^{48} \text{ erg}$  is deposited initially in the central region of  $r < 6.6 \times 10^8 \text{ cm}$ . The uniform density is set to be  $\rho = 1 \text{ g cm}^{-3}$ . We put a tiny specific internal energy ( $\epsilon = 10^{-8} \times c^2 \text{ erg g}^{-1}$ ) uniformly except for the central region mentioned above for numerical reasons. We adopt the  $\gamma$ -law EOS with  $\gamma = 4/3$ . We impose the free-boundary condition both for the inner and outer boundaries. Although all  $\theta$  derivatives vanish initially, they may evolve with time by numerical errors, and we set 60 uniform angular grid points for  $0^\circ \leq \theta \leq 90^\circ$ . We impose axisymmetry and equatorial symmetry on the  $z$ -axis and equatorial plane, respectively. We vary the resolution of the second level mesh to check the numerical convergence. The computations are terminated at  $t = 20$  s.

Figure 16 shows the numerical results (green dots) on the  $z$ -axis together with the analytical solutions (red lines). From left to right, different resolutions are employed for the second level mesh: three times, five times, and seven times finer in each coordinate direction than the first level mesh for the left, middle, and right columns, respectively. From top to bottom, the profiles of density, pressure, and radial velocity on the  $z$ -axis are displayed, respectively. Note that the horizontal axis is a radius normalized by the radius of the shock front,  $R_{\text{sh}} = 1.4 \times 10^{10} \text{ cm}$ . As is evident in this figure, our AMR code successfully reproduces the analytical solution with an increasing sharpness of the discontinuity as the second level mesh becomes finer.

### A.8. A Pulse Propagating through Meshes of Different Refinement Levels

In the AMR, there is a jump in resolution at the boundary between meshes of different refinement levels, which may produce unphysical waves. In order to make sure that the effect of the mesh boundary is negligible, we compute a pulse passing through the boundary adiabatically.

The initial pulse profile is the same as that employed in Appendix A.4. Since the present AMR code is based on the spherical grid, as mentioned earlier, we need in principle to reformulate the problem to accommodate a spherical wave. We can avoid this issue, however, by the so-called thin shell approximation, in which the radial range of the computational domain is taken to be much smaller than the radius itself and the coordinate curvature can be safely ignored. This convenient approximation has been widely used for plane-symmetric test problems on the spherical grid by Yamada (see, e.g., Yamada 1997). Here, we take  $r_* = 10^4$  and  $\Delta r_* = 1.35$  for the representative radius and thickness of the shell, respectively. The initial density profile is given by  $\rho_0(r - r_*)$  in Equation (A1). We assume that all  $\theta$  derivatives vanish initially. We employ a uniform angular mesh with 10 grid points in  $0^\circ \leq \theta \leq 0.5$ . We impose axisymmetry on the  $z$ -axis and adopt the free-boundary



**Figure 16.** Computed profiles of density (top panels), pressure (middle panels), and radial velocity (bottom panels) together with the exact solution (red lines) for the Sedov–Taylor problem. The AMR resolution becomes higher from left to right. (A color version of this figure is available in the online journal.)

condition at  $\theta = 0.5$ . The radial extent of the computational domain is  $-0.35 + r_* \leq r \leq 1 + r_*$  and is covered by a uniform mesh with 210 radial grid points. For the inner region of  $-0.35 + r_* \leq r \leq 0.3 + r_*$ , we deploy a second level mesh that is three times finer than the first level mesh in each coordinate direction.

Figure 17 shows the numerical evolution of the pulse. No artificial waves are discernible when the pulse passes over the boundary ( $r = 0.3 + r_*$ ) between the meshes of different refinement levels (cf. Figure 11). Although the post-pulse state is not identical to the reference state, the difference (mainly caused by the grid curvature) is negligible (only  $\sim 1\%$ ).

In the above run, the pulse is initially located in the region covered by the mesh of a higher refinement level and moves to the region of a lower refinement level. We also run a simulation in the opposite case, i.e., the pulse is initially put in the region of a lower refinement level (or the outer region) and moves to the inner region, which is covered by the mesh of a higher refinement level. This is realized by setting the initial density profile as  $\rho_0(r - r_* - 0.7)$  in Equation (A1) and determining the velocity distribution so that the Riemann invariant  $J_+ = \text{const}$  in Equation (A3) should be constant. The reference state and the

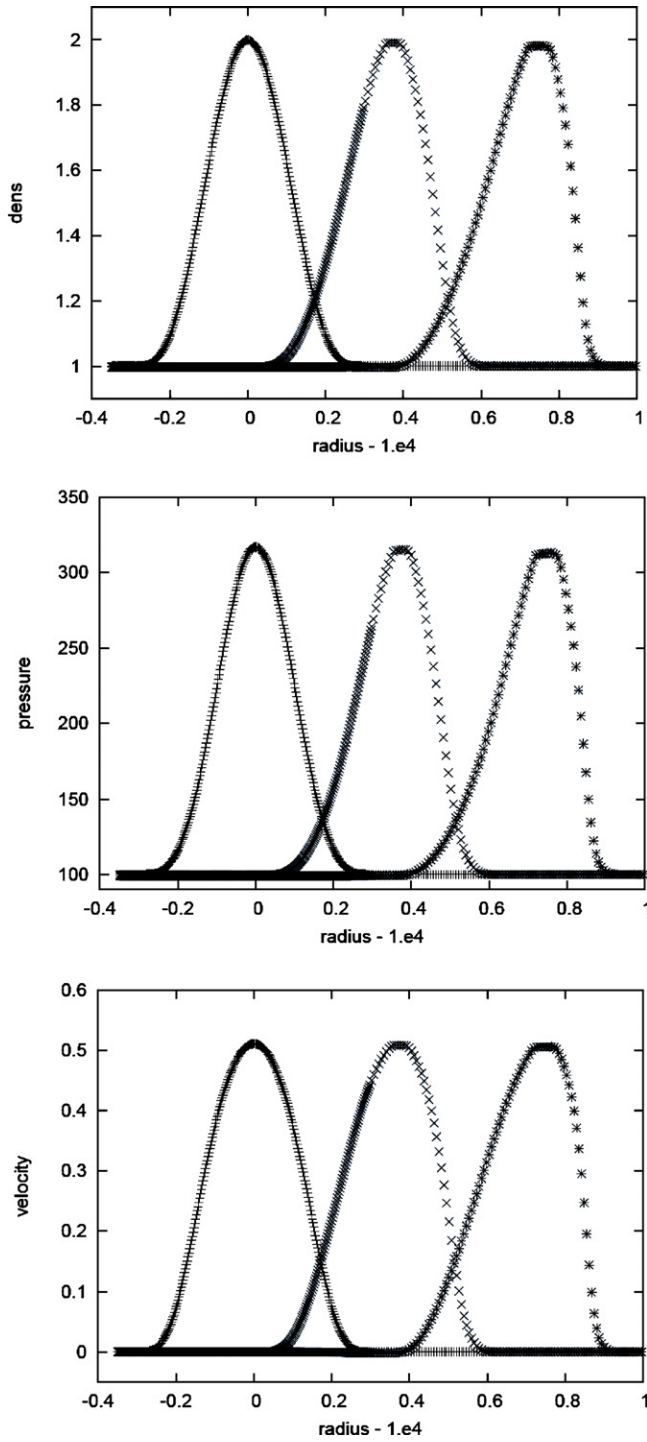
amplitude and width of the pulse are unchanged. The numerical grids are also the same as above.

Figure 18 shows the numerical results for the inward-moving pulse. Just as in the first case, the pulse passes through the mesh boundary, producing no discernible artificial wave. As expected, the pulse profile at the end of computation is a mirror image of the one for the outward-moving pulse. These test results demonstrate the good behavior of our AMR code at the mesh boundary.

#### A.9. Axisymmetric, Relativistic Jet Propagation in a Uniform Matter

The last test is meant to investigate the effect of AMR resolution on relativistic jet propagations and has been frequently used in the literature. The computational domain covers the region  $0.01 \leq r \leq 0.5$  and  $0^\circ \leq \theta \leq 90^\circ$ . Axisymmetry and equatorial symmetry are assumed, and a uniform mesh with 150 radial grid points and 60 angular grid points is adopted as the first level mesh. We perform two simulations with different AMR resolutions: the second level meshes are three times and nine times finer than the first level mesh, respectively. The relativistic jet is injected from the inner boundary by hand into

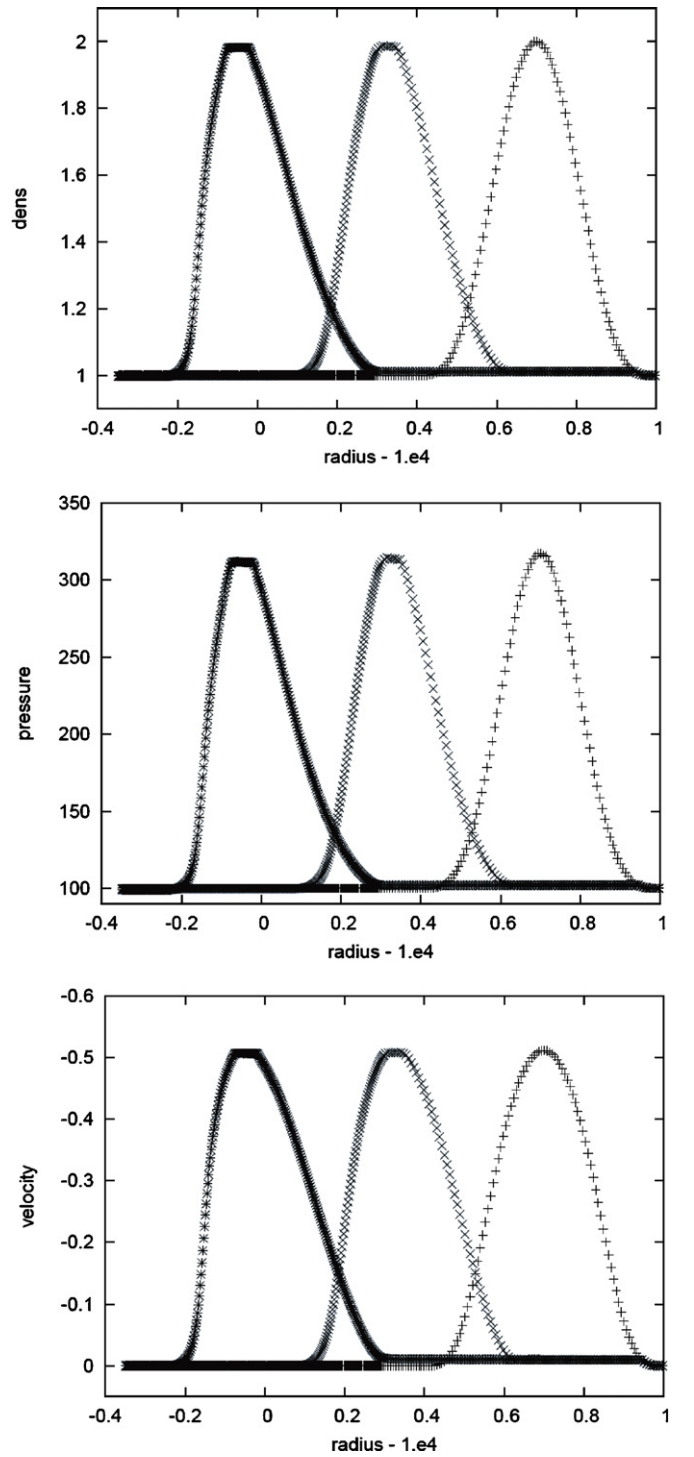




**Figure 17.** Computed profiles of density (top panel), pressure (middle panel), and radial velocity (bottom panel) at  $t = 0, 0.4$ , and  $0.8$  for the right-moving pulse. The mesh boundary is located at  $r - 10^4 = 0.3$ .

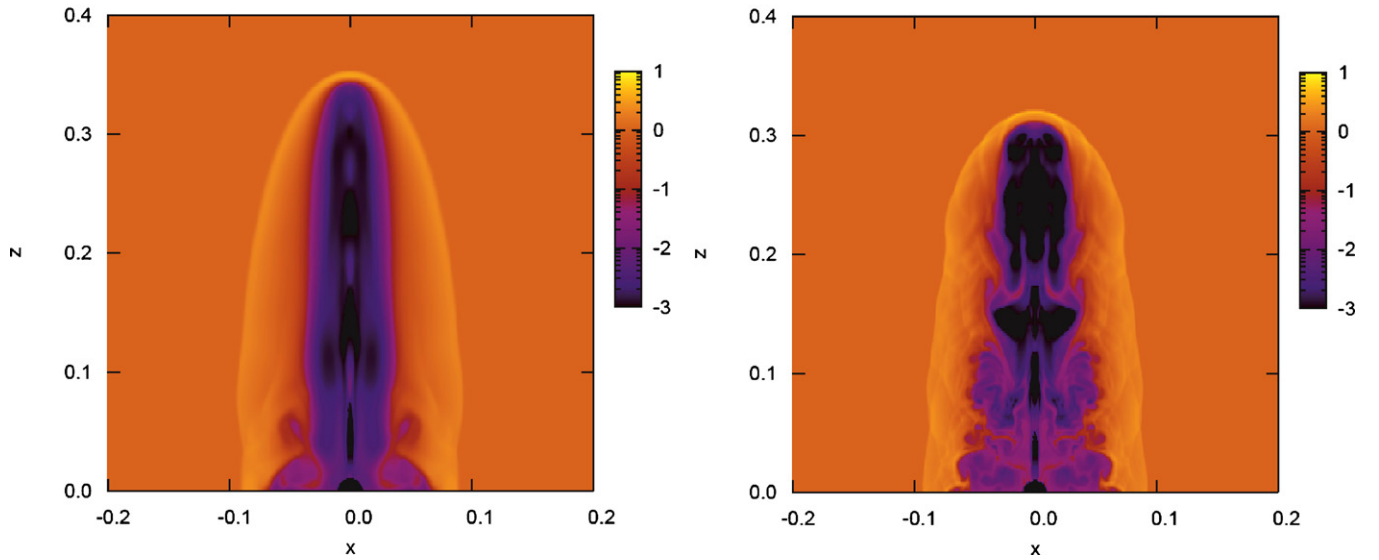
the uniform medium. The injection parameters are  $\rho_{0b} = 0.01$ ,  $p_b = 1.70 \times 10^{-4}$ , and  $v_b = 0.99$ . We employ  $\gamma$ -law EOS with  $\gamma = 5/3$ . The injection parameters give the Mach number of  $M_b = 6$ . The half-opening angle of the jet is chosen as  $\theta_{\text{hop}} = 9^\circ$ . The reference state has a density and pressure of  $\rho_{\text{am}} = 1.0$  and  $p_{\text{am}} = 1.70 \times 10^{-4}$ , respectively. Note that the ambient pressure is the same as the jet pressure. The simulation is terminated at  $t = 2$ .

Figure 19 shows the density contours at the end of the computation,  $t = 2$ , for the two different AMR resolutions.



**Figure 18.** Same as Figure 17 but for the left-moving pulse.

The propagation of the forward shock wave and global structure are not very different between the two cases. It is evident that the higher resolution captures more complex internal structures. It is well known that the internal jet structure never converges as the numerical resolution gets better. This is due to the Kelvin–Helmholtz instability, for which the growth rate is greater for shorter wavelengths. Indeed, the internal structures are very different between the two runs. The obtained numerical results in this test are qualitatively consistent with others in the literature (see, e.g., Figure 11 in Zhang & MacFadyen 2006).



**Figure 19.** Axisymmetric, relativistic jet propagations in a uniform medium. The density contours at  $t = 2$  are displayed. The left panel shows the result for the case, in which the second level mesh is three times finer than the first level mesh. The right panel gives the result when a nine times finer second level mesh is employed. (A color version of this figure is available in the online journal.)

**Table 2**

Numerical Errors for Different Resolutions in the 2D Isentropic-flow Problem

Number of Grid Points	$\delta\rho_0$ (%)	Convergence Rate ( $\alpha$ )
$48 \times 64$	0.90	...
$96 \times 128$	0.24	1.93
$192 \times 256$	$6.17\text{E-}2$	1.93
$384 \times 512$	$1.24\text{E-}2$	2.32
$768 \times 1024$	$2.70\text{E-}3$	2.20

**Notes.** The errors of density are evaluated at  $t = 2.4$ . See the text for the definition of  $\delta\rho_0$ . In the rightmost column, the powers in the expression  $\delta\rho_0 \propto N^{-\alpha}$ , where  $N$  denotes the number of grids, are given.

## REFERENCES

- Abdo, A. A., et al. 2009, *ApJ*, **706**, L138
- Abramowicz, M. A., Novikov, I. D., & Paczynski, B. 1991, *ApJ*, **369**, 175
- Aloy, M. A., Müller, E., Ibáñez, J. M., Martí, J. M., & MacFadyen, A. 2000, *ApJ*, **531**, L119
- Blinnikov, S. I., Dunina-Barkovskaya, N. V., & Nadyozhin, D. K. 1996, *ApJS*, **106**, 171
- Campana, S., et al. 2006, *Nature*, **442**, 1008
- Del Zanna, L., & Bucciantini, N. 2002, *A&A*, **390**, 1177
- Falk, S. W. 1978, *ApJ*, **225**, L133
- Guirrec, S., et al. 2010, *ApJ*, **727**, L33
- Hachisu, I. 1986, *ApJS*, **61**, 479
- Ioka, K. 2010, *Prog. Theor. Phys.*, **124**, 667
- Ioka, K., Murase, K., Toma, K., Nagataki, S., & Nakamura, T. 2007, *ApJ*, **670**, L77
- Kiuchi, K., Nagakura, H., & Yamada, S. 2010, *ApJ*, **717**, 666
- Klein, R. I., & Chevalier, R. A. 1978, *ApJ*, **223**, L109
- Kotake, K., Sato, K., & Takahashi, K. 2006, *Rep. Prog. Phys.*, **69**, 971
- Kumar, P., & Narayan, R. 2009, *MNRAS*, **395**, 472
- Kurganov, A., & Tadmor, E. 2000, *J. Comput. Phys.*, **160**, 241
- Lazar, A., Nakar, E., & Piran, T. 2009, *ApJ*, **695**, L10
- Lazzati, D. 2005, *MNRAS*, **357**, 722
- Lazzati, D., & Begelman, M. C. 2005, *ApJ*, **629**, 903
- Lazzati, D., Morsony, B. J., & Begelman, M. C. 2009, *ApJ*, **700**, L47
- Lindner, C. C., Milosavljević, M., Couch, S. M., & Kumar, P. 2010, *ApJ*, **713**, 800
- MacFadyen, A. I., & Woosley, S. E. 1999, *ApJ*, **524**, 262
- MacFadyen, A. I., Woosley, S. E., & Heger, A. 2001, *ApJ*, **550**, 410
- Matzner, C. D., & McKee, C. F. 1999, *ApJ*, **510**, 379
- Milosavljevic, M., Lindner, C. C., Shen, R., & Kumar, P. 2010, arXiv:1007.0763
- Mizuta, A., & Aloy, M. A. 2009, *ApJ*, **699**, 1261
- Mizuta, A., Kino, M., & Nagakura, H. 2010a, *ApJ*, **709**, L83
- Mizuta, A., Nagataki, S., & Aoi, J. 2010b, arXiv:1006.2440
- Mizuta, A., Yamasaki, T., Nagataki, S., & Mineshige, S. 2006, *ApJ*, **651**, 960
- Morsony, B. J., Lazzati, D., & Begelman, M. C. 2007, *ApJ*, **665**, 569
- Nagakura, H., & Yamada, S. 2008, *ApJ*, **689**, 391
- Paczynski, B. 1998, *ApJ*, **494**, L45
- Pe'er, A. 2008, *ApJ*, **682**, 463
- Piran, T. 2004, *Rev. Mod. Phys.*, **76**, 1143
- Pons, J. A., Ma Martí, J., & Müller, E. 2000, *J. Fluid Mech.*, **422**, 125
- Rezzolla, L., & Zanotti, O. 2002, *Phys. Rev. Lett.*, **89**, 114501
- Ryde, F., et al. 2010, *ApJ*, **709**, L172
- Soderberg, A. M., et al. 2008, *Nature*, **454**, 246
- Toma, K., Wu, X.-F., & Meszaros, P. 2010, arXiv:1002.2634
- Tominaga, N., Maeda, K., Umeda, H., Nomoto, K., Tanaka, M., Iwamoto, N., Suzuki, T., & Mazzali, P. A. 2007, *ApJ*, **657**, L77
- Waxman, E., Mészáros, P., & Campana, S. 2007, *ApJ*, **667**, 351
- Woosley, S. E. 1993, *ApJ*, **405**, 273
- Woosley, S. E., & Bloom, J. S. 2006, *ARA&A*, **44**, 507
- Woosley, S. E., & Heger, A. 2006, *ApJ*, **637**, 914
- Yamada, S. 1997, *ApJ*, **475**, 720
- Yonetoku, D., Murakami, T., Nakamura, T., Yamazaki, R., Inoue, A. K., & Ioka, K. 2004, *ApJ*, **609**, 935
- Zhang, W., & MacFadyen, A. I. 2006, *ApJS*, **164**, 255
- Zhang, W., Woosley, S. E., & Heger, A. 2004, *ApJ*, **608**, 365
- Zhang, W., Woosley, S. E., & MacFadyen, A. I. 2003, *ApJ*, **586**, 356